

An electromechanics-driven fluid dynamics model for the simulation of the whole human heart

Alberto Zingaro^{a,b,*}, Michele Bucelli^a, Roberto Piersanti^a, Francesco Regazzoni^a, Luca Dede^a, Alfio Quarteroni^{a,c}

^a*MOX, Laboratory of Modeling and Scientific Computing, Dipartimento di Matematica, Politecnico di Milano, Piazza Leonardo da Vinci 32, 20133, Milano, Italy*

^b*ELEM BioTech, Pier07, Calle Laietana, 26, 08003, Barcelona, Spain*

^c*Institute of Mathematics, École Polytechnique Fédérale de Lausanne, Station 8, Av. Piccard, CH-1015 Lausanne, Switzerland (Professor Emeritus)*

Abstract

We introduce a multiphysics and geometric multiscale computational model, suitable to describe the hemodynamics of the whole human heart, driven by a four-chamber electromechanical model. We first present a study on the calibration of the biophysically detailed RDQ20 active contraction model (Regazzoni *et al.*, 2020) that is able to reproduce the physiological range of hemodynamic biomarkers. Then, we demonstrate that the ability of the force generation model to reproduce certain microscale mechanisms, such as the dependence of force on fiber shortening velocity, is crucial to capture the overall physiological mechanical and fluid dynamics macroscale behavior. This motivates the need for using multiscale models with high biophysical fidelity, even when the outputs of interest are relative to the macroscale. We show that the use of a high-fidelity electromechanical model, combined with a detailed calibration process, allows us to achieve a remarkable biophysical fidelity in terms of both mechanical and hemodynamic quantities. Indeed, our electromechanical-driven CFD simulations – carried out on an anatomically accurate geometry of the whole heart – provide results that match the cardiac physiology both qualitatively (in terms of flow patterns) and quantitatively (when comparing *in silico* results with biomarkers acquired *in vivo*). Moreover, we consider the pathological case of left bundle branch block, and we investigate the consequences that an electrical abnormality has on cardiac hemodynamics thanks to our multiphysics integrated model. The computational model that we propose can faithfully predict a delay and an increasing wall shear stress in the left ventricle in the pathological condition. The interaction of different physical processes in an integrated framework allows us to faithfully describe and model this pathology, by capturing and reproducing the intrinsic multiphysics nature of the human heart.

1. Introduction

The study of cardiac blood flows aims at enhancing the knowledge of heart physiology, assessing pathological conditions, and possibly improving clinical treatments and therapeutics. In the last decades, the role of mathematical models in the study of cardiac hemodynamics has increasingly gained relevance, for their non-invasiveness and flexibility with respect to geometries and flow conditions [1, 2, 3, 4, 5, 6, 7, 8, 9]. Computational Fluid Dynamics (CFD) is largely employed to provide a detailed description of cardiac flows and to estimate hemodynamic indicators, like e.g., the wall shear stress, that standard image-based techniques might not capture [1]. A biophysically detailed mathematical model of cardiac hemodynamics entails the complex interplay among different processes such as the interaction with cardiac electromechanics (EM), valve dynamics, transition-to-turbulence effects, and coupling with the surrounding circulation. Furthermore, while the literature about CFD models of the left ventricle [10, 11, 12, 13, 4, 3], left atrium [14, 15, 8, 16, 17, 18, 19, 20, 21, 22, 23] and left heart [9, 24, 25, 26, 27, 1, 28, 29, 30, 31] is relevant, the fluid dynamics simulation of the right heart is the subject of few works [32], and they often focus on the sole right ventricle [33, 34, 35], neglecting the right atrium description. Conversely, whole-heart fluid dynamics modeling is a much more challenging topic and has been addressed only recently in a few works [36, 37, 38, 39, 40, 41]. As a matter of fact, to the best of our knowledge, hemodynamics simulations of the whole heart are presented only in the following papers. A four-chamber CFD model is proposed by the Siemens group in [36]: the displacement of cardiac walls is obtained from patient-specific images and, since the left and right sides are not connected to the surrounding circulation, they performed simulations separately on the two parts. In [37], the authors introduce

*Corresponding author: email: alberto.zingaro@polimi.it

a Fluid Structure Interaction (FSI) simulation of the whole heart based on the UT-Heart simulator developed at the University of Tokyo. Moreover, FSI simulations of the whole heart have been performed in the context of the Living Heart Project [38]. A sequentially-coupled FSI model of the whole heart is devised in [39], showing that few iterations of the solver are needed to reach convergence in terms of mechanical indicators. Recently, a patient-specific whole-heart CFD model is introduced in [40], consisting of the Navier-Stokes-Brinkman equations [42] with prescribed boundary motion and, similarly to [36], simulations of the left and right parts are carried out separately. Finally, a GPU-accelerated fully-coupled electro-mechano-fluid computational model of the whole heart, based on the immersed boundary method, is presented in [41].

In this paper, we propose a four-chamber electromechanical-driven fluid dynamics model, which is characterized by a remarkable biophysical fidelity and able to faithfully describe potential pathologies. Moreover, to improve the virtual representation of the heart physiology enabled by our model, we present a careful manual calibration of the active contraction model (at the cellular level) to reproduce mechanical and hemodynamic biomarkers in the physiological range.

The blood flow in heart chambers is commonly modeled by Navier-Stokes equations for Newtonian fluids [43]. A crucial aspect in heart flows modeling is the treatment of boundary displacement, i.e. the way the deformation of cardiac walls is accounted for into the model. The boundary displacement can be the solution of a suitable mathematical model for the dynamics of the walls, fully coupled to the fluid dynamics model in an FSI framework, by imposing geometric, kinematic, and dynamic coupling conditions at the fluid-solid interface. The motion of the myocardium is in turn driven by muscular EM, resulting in a coupled electro-mechano-fluid problem (see e.g. [9, 24, 25, 44, 45, 46, 47, 48]). This approach, while being very comprehensive and physically motivated, entails a significant computational effort, due to the number of subsystems involved and to the non-linearity induced by the coupling. To mitigate this large computational cost, the boundary displacement can be prescribed as a datum, without any feedback from the fluid flow, in a CFD modeling framework. The displacement may be prescribed by suitable analytical laws [4, 26, 3, 16, 49, 50, 11, 13, 17, 51], from patient-specific image-based reconstructions [5, 7, 1, 15, 14, 8, 29, 31, 30, 32], or else obtained from a previously performed EM simulation [52, 6, 2, 2, 53, 27, 54]. The latter corresponds to a one-way coupled approach between EM and CFD, since only the kinematic coupling is enforced, without foreseeing any dynamic feedback from the fluid to the structure problem. This approach is also referred to as “kinematic uncoupling” [2, 55].

A critical issue in 3D cardiovascular hemodynamics modeling is the prescription of boundary conditions at inlet and outlet sections, since boundary data are generally unavailable, but also because the circulatory system is a closed-loop network and the mathematical model should account for it. A possible approach is the so called *geometric multiscale modeling* [56]: the region of interest (in our case, the whole-heart) is described by a 3D model, while the remaining part of the circulation is addressed by means of lumped-parameter models, as 0D [57, 58, 56, 59, 60], or 1D [56, 61, 62, 63, 46]. The geometric multiscale modeling allows to account for the mutual interaction between the heart and the circulatory system, especially if the lumped parameter model provides a closed-loop description of the vascular network, as done in [27, 64, 65, 57, 66, 67].

An additional key aspect in cardiac CFD simulations is the modeling of the cardiac valves. In principle, these can be treated by considering a structural model for the solid (leaflets of the valve and possibly its chordae tendinae) and a fluid dynamics model for the surrounding blood flow. This approach yields a coupled FSI model of the blood-valve system [68, 69, 70, 71, 72, 73, 25, 74, 75, 76], characterized by contact phenomena and fast dynamics. Thus, FSI valve models are commonly associated to a huge computational burden, to be added to the overall cost of the heart CFD simulation. To avoid this large computational cost, the effects of the valves in the blood can be surrogated by relying on reduced models for the valve dynamics [77, 5, 78, 79, 80, 40, 53].

Our computational model of the whole human heart encompasses the main features of the cardiac hemodynamics: EM, cardiac valves, transition-to-turbulence effects, and interplay with the external circulation. Indeed, our fluid model is driven by the four-chamber EM model recently proposed in [64]. The multiphysics model is fully coupled to the external circulation described by a lumped-parameter model, extending the computational framework we introduced in [27] to the case of four-chamber CFD simulations. We carry out numerical simulations on an anatomically accurate geometry of the heart, obtaining results that are quantitatively in agreement with data from the medical literature and qualitative faithfully in terms of blood flow patterns. In this respect, we analyze the role played by the highly biophysically detailed RDQ20 active contraction model [81] on relevant hemodynamic quantities. Indeed, since the electromechanical displacement drives the deformation of cardiac chambers for the CFD simulation, its calibration is fundamental towards faithfully reproducing heart physiology. As shown in [64], the parameters of the active contraction model play a significant role in determining the flow rates across cardiac valves, which have a dramatic impact on the CFD simulation, both in terms of macroscopic indicators and overall flow distribution. Therefore, we present a detailed manual calibration of the active force generation model,

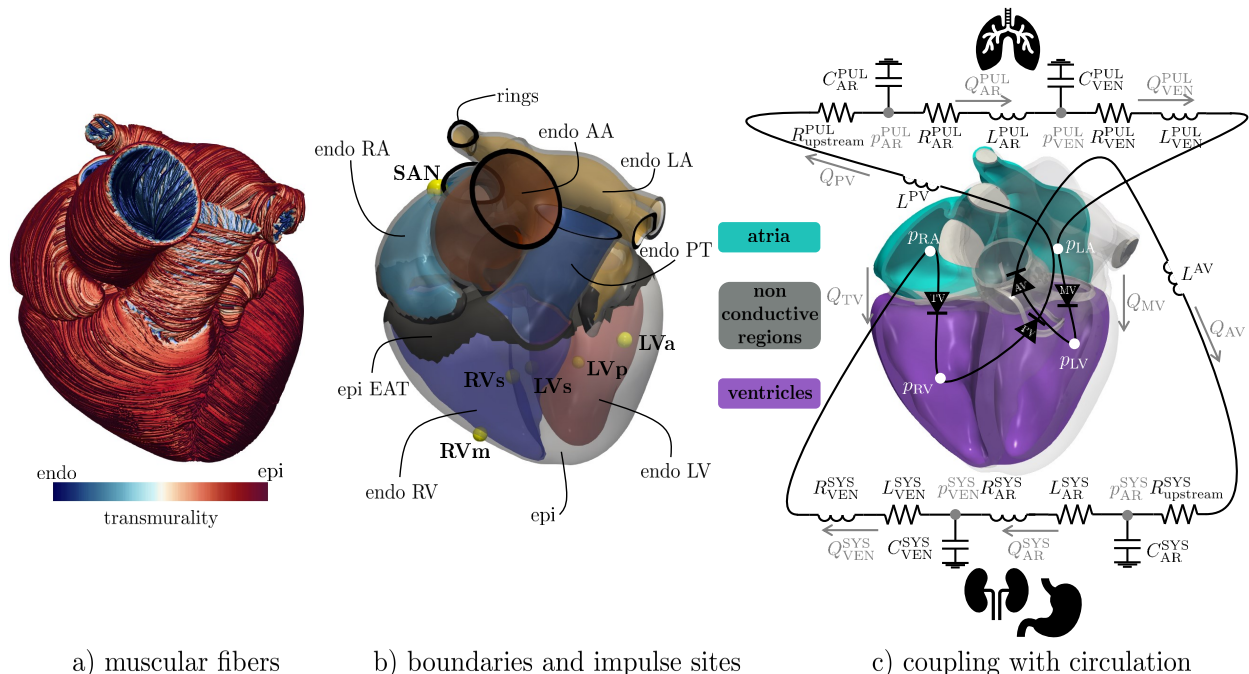


Figure 1: The whole-heart EM model: a) cardiac muscular fibers, (b) boundaries and impulse sites (yellow spheres with bold labels), (c) coupling with circulation and we highlight the three main regions of the EM model (atria, ventricles and non-conductive regions).

validating our results on several macroscopic heartbeat indicators such as stroke volumes, ejection fractions, peak flowrates and, consequently, also in terms of blood velocities computed in the CFD simulation. Our sensitivity analysis highlights that microscopic features of the RDQ20 model have a large impact on the macroscopic characteristics of the heartbeat. Then, we show that our detailed computational model can improve the understanding of the impact of the Left Bundle Branch Block (LBBB) pathology [82] on CFD biomarkers, by capturing the effects that an electrophysiological abnormality has on different physical processes behind the heart activity, henceforth allowing to capture the intrinsic multiphysics nature of the cardiac function. This paper represents one the few examples in the literature on the modeling and simulation of the whole heart hemodynamics. Moreover, to the best of our knowledge, this is the first work in which the 3D whole heart fluid dynamics model is also coupled to a lumped-parameter closed-loop circulation model.

This paper is organized as follows: in Section 2, we introduce the mathematical models employed for the EM, fluid dynamics and circulation problems. Section 3 is devoted to the description of the numerical methods for each subproblem and to the strategies used for their coupling. In Section 4, we present numerical results on a realistic whole-heart geometry, in both physiological and pathological conditions. Finally, limitations and conclusions follow in Section 5 and Section 6, respectively.

2. Mathematical model

In this section, we introduce the mathematical model. Specifically, the EM model is briefly described in Section 2.1 and the whole-heart fluid domain is defined in Section 2.2. We present our approach suitable to deal with the domain deformation in Section 2.3, the fluid dynamics model in Section 2.4, and its coupling with the external circulation in Section 2.5.

2.1. The whole-heart electromechanical model

The whole-heart EM is based on a comprehensive and biophysically detailed computational model that we recently presented in [64]. More precisely, we consider a 3D description of cardiac EM in all the four-chambers and a 0D representation of the complete circulatory system, including the cardiac blood hemodynamics [65, 83], as we display in Figure 1c.

The whole-heart EM model includes a detailed myocardial fiber architecture built upon a total-heart Laplace-Dirichlet Rule-Based Method [84], which couples together different methods for the atria [85] and the ventricles [86], to properly reproduce the characteristic features of the cardiac fiber bundles in all the four-chambers [85], see Figure 1a.

Cardiac electrophysiology is described by means of the monodomain equation equipped with no-flux Neumann boundary conditions [87] and endowed with the following human ionic models: ten Tusscher-Panfilov for the ventricles [88] and Courtemanche-Ramirez-Nattel for the atria [89]. Furthermore, the arterial vessels and the atrio-ventricular basal plane are assumed to be non-conductive regions, whence electrically isolating the atria from the ventricles [64]. Finally, the cardiac conduction system is substituted by a series of spherical electrical impulses, originating from the sino-atrial node (SAN) and ending into the left and right ventricular endocardia which, combined with a fast endocardial layer, surrogates the effect of the Purkinje network [90, 64], as we show in Figure 1b.

The sarcomere mechanical activation is based on the biophysically detailed RDQ20 active contraction model [81], properly calibrated for both atria [91] and ventricles [92]. The RDQ20 is able to represent in detail the sophisticated microscopic active force generation mechanisms, taking place at the scale of sarcomeres [92]. Moreover, to differentiate the active tension in left and right ventricles, we consider a spatially heterogeneous active tension [83], i.e. defined in relation to a normalized inter-ventricular distance. Notably, we set the active tension in the right ventricle at 70% of that in the left ventricle, whereas we keep the same contractility between left and right atrium.

The myocardial tissue mechanics is described by the momentum balance equation under the hyperelasticity assumption [93]. We employ, for the active part, an orthotropic active stress formulation [83], which surrogates the contraction caused by dispersed myofibers [94], and, for the passive behavior, specific mechanical constitutive laws and model parameters for the different cardiac region: the Usyk constitutive law for both the atria and the ventricles [95] and a Neo-Hookean strain energy density function for the atrio-ventricular basal plane and the vessels [93]. Finally, a nearly incompressible formulation is enforced with a penalty method [64]. Concerning the mechanical boundary conditions, we consider: i) generalized Robin boundary conditions on the epicardium, surrogating both the presence of the pericardium and also the epicardial adipose tissue, crucial for reproducing the correct downward and upward movement of the atrio-ventricular basal plane [64]; ii) normal stress boundary conditions on the four-chamber endocardia and vessel endothelia to account for the pressures exerted by the blood, where the endocardium and endothelium fluid pressures are given by the coupling between the mechanical and the circulation problems [65, 83, 64]; iii) homogeneous Dirichlet boundary condition on all the artificial rings where we cut the computational domain, since the arteries and atrial veins can be considered fixed here [64], as displayed in Figure 1b. When setting boundary conditions on the epicardial boundary, we opted for reduced values of normal stiffness and normal damping on the epicardial adipose tissue (EAT, see Figure 1b). This choice allows the ventricular base to be more free to move, as well as the appendages of the left and the right atria.

The whole-heart 3D EM model is fully coupled with a 0D closed-loop lumped parameters model for the blood hemodynamics through the entire cardiovascular network. Systemic and pulmonary circulations are modeled using resistance-inductance-capacitance circuits (both for the arterial and venous part) and non-ideal diodes stand for the heart valves [65]. In Figure 1c we give a graphical representation of the 3D-0D model. The coupling between the 0D and 3D EM models is achieved by introducing volume-consistency coupling conditions, where the pressures of all the four-chambers act as Lagrange multipliers associated with the introduced volume constraints [65, 83].

The most relevant feedbacks, representing the interactions among electric signal propagation, the cardiac tissue deformation and contraction, and the circulatory system, are modelled inside the whole-heart EM model [64]. These include e.g. the mechano-electric feedback [96] (between electrophysiology and mechanics) and the fibers-stretch and fibers-stretch-rate feedbacks [97] (between mechanics and the active contraction model).

For the full set of equations of the whole-heart EM model, we refer to [64, 83, 65].

In this paper, the whole-heart EM model serves as unidirectional input for the fluid dynamics problem as we better detail in Section 2.3 and Section 2.4.

2.2. The whole-heart fluid domain

Let Ω_t be the fluid domain at time $t > 0$ bounded with a sufficiently regular boundary $\Gamma_t \equiv \partial\Omega_t$ and let $(0, T)$ be the temporal domain, with T the final time. From a fluid dynamics view point, the whole-heart fluid domain Ω_t is topologically disjoint and split into left heart (LH, Ω_t^{LH}) and right heart (RH, Ω_t^{RH}), as we show in Figure 2: $\Omega_t = \Omega_t^{\text{RH}} \cup \Omega_t^{\text{LH}}$, with $\overline{\Omega}_t^{\text{RH}} \cap \overline{\Omega}_t^{\text{LH}} = \emptyset$. Specifically,

$$\begin{aligned}\overline{\Omega}_t^{\text{RH}} &= \overline{\Omega}_t^{\text{RA}} \cup \overline{\Omega}_t^{\text{TV}} \cup \overline{\Omega}_t^{\text{RV}} \cup \overline{\Omega}_t^{\text{PV}} \cup \overline{\Omega}_t^{\text{PT}}, \\ \overline{\Omega}_t^{\text{LH}} &= \overline{\Omega}_t^{\text{LA}} \cup \overline{\Omega}_t^{\text{MV}} \cup \overline{\Omega}_t^{\text{LV}} \cup \overline{\Omega}_t^{\text{AV}} \cup \overline{\Omega}_t^{\text{AO}},\end{aligned}$$

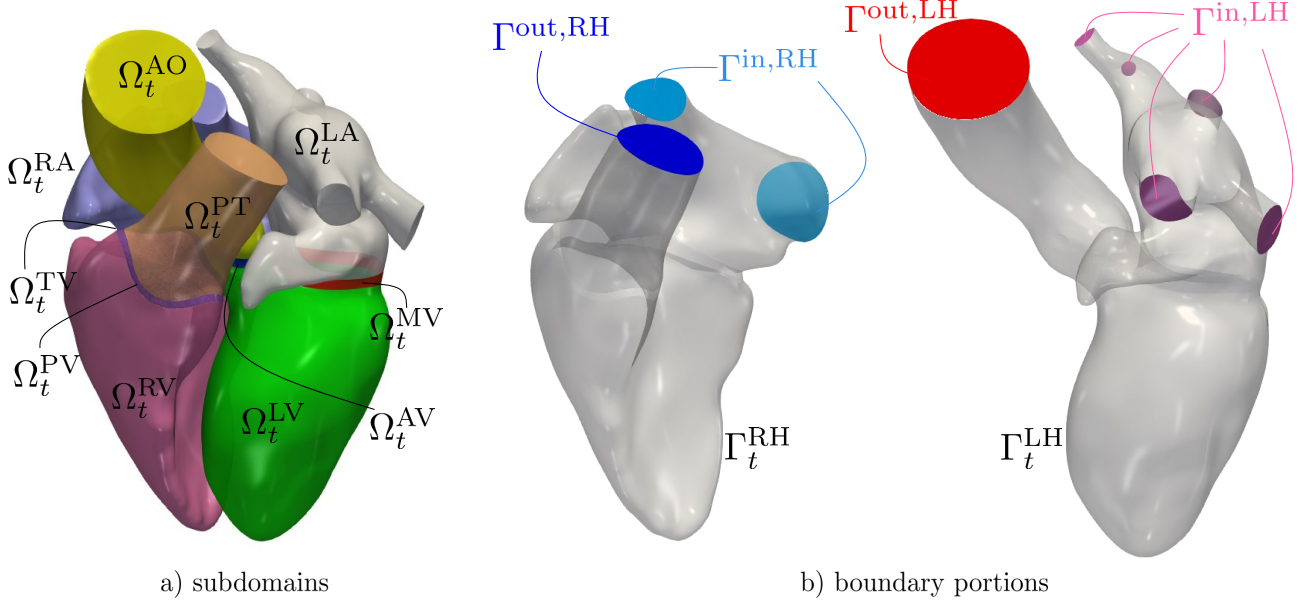


Figure 2: The whole-heart fluid domain: (a) subdomains composing the whole heart; (b) boundary portions (the left and right part are separated for visualization purposes).

where Ω_t^{RA} , Ω_t^{RV} , Ω_t^{PT} are the right atrium (RA), right ventricle (RV) and pulmonary trunk (PT) subdomains, and Ω_t^{LA} , Ω_t^{LV} , Ω_t^{AO} the left atrium (LA), left ventricle (LV) and aorta (AO) subdomains. Moreover, Ω_t^{TV} , Ω_t^{PV} , Ω_t^{MV} , Ω_t^{AV} are the subdomains representing the rings of the tricuspid valve (TV), pulmonary valve (PV), mitral valve (MV) and aortic valve (AV). Analogously, we partition the boundary of the whole-heart domain as $\Gamma_t = \Gamma_t^{\text{RH}} \cup \Gamma_t^{\text{LH}}$, with $\Gamma_t^{\text{RH}} \cap \Gamma_t^{\text{LH}} = \emptyset$. In particular, as displayed in Figure 2b,

$$\Gamma_t^{\text{RH}} = \Gamma^{\text{out,RH}} \cup \Gamma^{\text{in,RH}} \cup \Gamma_t^{\text{w,RH}},$$

with $\Gamma^{\text{in,RH}}$ the inlet sections of the superior and inferior venae cavae, $\Gamma^{\text{out,RH}}$ the outlet section of the pulmonary trunk, and $\Gamma_t^{\text{w,RH}}$ the endocardium of the RH. In an analogous fashion, on the left part:

$$\Gamma_t^{\text{LH}} = \Gamma^{\text{out,LH}} \cup \Gamma^{\text{in,LH}} \cup \Gamma_t^{\text{w,LH}},$$

with $\Gamma^{\text{in,LH}}$ the five inlet sections of the four pulmonary veins, $\Gamma^{\text{out,LH}}$ the outlet section of the aorta, and $\Gamma_t^{\text{w,LH}}$ the LH endocardium.

2.3. The fluid domain displacement problem

To represent the deformation of the domain over time, we introduce a fixed reference configuration $\hat{\Omega} \subset \mathbb{R}^3$, such that the domain in current configuration Ω_t is defined at any $t \in (0, T)$ as

$$\Omega_t = \{\mathbf{x} \in \mathbb{R}^3 : \mathbf{x} = \hat{\mathbf{x}} + \mathbf{d}(\hat{\mathbf{x}}, t), \hat{\mathbf{x}} \in \hat{\Omega}\},$$

where $\mathbf{d} : \hat{\Omega} \times (0, T)$ is the displacement of the domain, and is obtained it by solving the following harmonic extension problem:

$$\begin{cases} -\nabla \cdot (s \nabla \mathbf{d}) = \mathbf{0} & \text{in } \hat{\Omega} \times (0, T), \\ \mathbf{d} = \mathbf{d}^{\partial\Omega}(\mathbf{x}, t) & \text{on } \partial\hat{\Omega} \times (0, T). \end{cases} \quad (1a) \quad (1b)$$

In Equation (1), $\mathbf{d}^{\partial\Omega} : \partial\hat{\Omega} \times (0, T)$ is the boundary displacement, computed by restricting the solution of the EM simulation to the endocardium and the endothelium. Furthermore, $s : \hat{\Omega} \times (0, T) \rightarrow \mathbb{R}$ is a space-dependent scalar field introduced to avoid distortion of mesh elements. Specifically, we use the boundary-based stiffening approach proposed in [98]. We denote the fluid domain displacement problem Equation (1) with the abridged notation

$$\mathcal{D}(\mathbf{d}, \mathbf{d}^{\partial\Omega}) = 0.$$

The EM simulation is solved with a significantly larger timestep than the CFD one. Therefore, the boundary displacement $\tilde{\mathbf{d}}^{\partial\Omega}$ is only available for some times t_k , $k = 0, 1, \dots, N_{\text{EM}}$, although the domain displacement \mathbf{d} is needed with a finer temporal resolution. Thus, problem (1) is solved for all times t_k , and then we construct a displacement field $\tilde{\mathbf{d}}(t) : \tilde{\Omega} \times (0, T) \rightarrow \mathbb{R}^3$ using smoothing splines approximation in time [99].

We compute the domain velocity by deriving the displacement in time as

$$\mathbf{u}^{\text{ALE}} = \frac{\partial \tilde{\mathbf{d}}}{\partial t} \text{ in } \Omega_t \times (0, T). \quad (2)$$

2.4. The Navier-Stokes equations in ALE framework with the RIIS model of the valves

We model the blood in the cardiac cavities as an incompressible, viscous and Newtonian fluid characterized by constant density ρ and constant dynamic viscosity μ . We therefore use the time-dependent incompressible Navier-Stokes equations expressed in an Arbitrary Lagrangian Eulerian (ALE) framework to account for the moving domain. We denote by $\mathbf{u} : \Omega_t \times (0, T) \rightarrow \mathbb{R}^3$ and $p : \Omega_t \times (0, T) \rightarrow \mathbb{R}$ the fluid velocity and pressure, respectively. Let σ be the Cauchy stress tensor, defined for incompressible, Newtonian and viscous fluids as $\sigma(\mathbf{u}, p) = -p\mathbf{I} + 2\mu\epsilon(\mathbf{u})$, with $\epsilon(\mathbf{u}) = \frac{1}{2}(\nabla\mathbf{u} + (\nabla\mathbf{u})^T)$ the strain-rate tensor.

We model the effects of cardiac valves in the fluid by means of the Resistive Immersed Implicit Surface (RIIS) method [77]. We consider four immersed surfaces Σ_k , with $k \in \mathcal{I}_v = \{\text{MV}, \text{AV}, \text{TV}, \text{PV}\}$ the set of valves. Each valve is characterized by a resistance coefficient R_k and a parameter ε_k representing the half thickness of the valve leaflets. The immersed surface is implicitly described by a signed distance function $\varphi_k : \Omega_t \times (0, T) \rightarrow \mathbb{R}$. With the RIIS method, we introduce the following penalty term to the momentum balance of the Navier-Stokes equations (expressed in ALE form):

$$\mathcal{R}(\mathbf{u}, \mathbf{u}^{\text{ALE}}) = \sum_{k \in \mathcal{I}_v} \frac{R_k}{\varepsilon_k} \delta_{\Sigma_k, \varepsilon_k}(\varphi_k) (\mathbf{u} - \mathbf{u}^{\text{ALE}} - \mathbf{u}_{\Sigma_k}).$$

\mathcal{R} penalizes the mismatch between the relative velocity $\mathbf{u} - \mathbf{u}^{\text{ALE}}$ and the velocity of the valves' leaflets \mathbf{u}_{Σ_k} , weakly imposing a kinematic coupling condition only. The resistive term is only acting on a tiny support around Σ_k , thanks to a smoothed Dirac delta function acting as multiplicative factor. We refer to [77] for its definition.

By defining with $\frac{\partial \mathbf{u}}{\partial t} = \frac{\partial \mathbf{u}}{\partial t} + (\mathbf{u}^{\text{ALE}} \cdot \nabla)\mathbf{u}$ the ALE derivative, the 3D fluid dynamics model of the whole heart reads:

$$\left\{ \begin{array}{ll} \rho \frac{\partial \mathbf{u}}{\partial t} + ((\mathbf{u} - \mathbf{u}^{\text{ALE}}) \cdot \nabla)\mathbf{u} + \nabla \cdot \sigma(\mathbf{u}, p) + \mathcal{R}(\mathbf{u}, \mathbf{u}^{\text{ALE}}) = \mathbf{0} & \text{in } \Omega_t \times (0, T), \quad (3a) \\ \nabla \cdot \mathbf{u} = 0 & \text{in } \Omega_t \times (0, T), \quad (3b) \\ \sigma(\mathbf{u}, p)\mathbf{n} = -p_{\text{RA}}^{\text{in}}\mathbf{n} & \text{on } \Gamma^{\text{in}, \text{RH}} \times (0, T), \quad (3c) \\ \sigma(\mathbf{u}, p)\mathbf{n} = -p_{\text{AR}}^{\text{PUL}}\mathbf{n} & \text{on } \Gamma^{\text{out}, \text{RH}} \times (0, T), \quad (3d) \\ \sigma(\mathbf{u}, p)\mathbf{n} = -p_{\text{LA}}^{\text{in}}\mathbf{n} & \text{on } \Gamma^{\text{in}, \text{LH}} \times (0, T), \quad (3e) \\ \sigma(\mathbf{u}, p)\mathbf{n} = -p_{\text{AR}}^{\text{SYS}}\mathbf{n} & \text{on } \Gamma^{\text{out}, \text{LH}} \times (0, T), \quad (3f) \\ \mathbf{u} = \mathbf{u}^{\text{ALE}} & \text{on } \Gamma_t^{\text{w}, \text{RH}} \cup \Gamma_t^{\text{w}, \text{LH}} \times (0, T). \quad (3g) \\ \mathbf{u} = \mathbf{u}_0 & \text{in } \Omega_0 \times \{0\}, \quad (3h) \end{array} \right.$$

where $p_{\text{RA}}^{\text{in}}$, $p_{\text{AR}}^{\text{PUL}}$, $p_{\text{LA}}^{\text{in}}$, $p_{\text{AR}}^{\text{SYS}}$ are the pressures arising from the coupling with the circulation model, as we detail in Section 2.5, and \mathbf{u}_0 is the initial velocity. We denote the 3D fluid dynamics model of the whole heart in Equation (3) by

$$\mathcal{F}(\mathbf{u}, p, \mathbf{u}^{\text{ALE}}) = 0.$$

2.5. Coupling with circulation

To account for the interplay between the heart's fluid dynamics and the hemodynamics of the surrounding circulation, we couple the cardiac CFD model to a 0D closed-loop model of the whole circulation proposed in [65]. Specifically, we extend to the whole heart the coupling strategy that we devised in [27] for the case of the sole left heart. We consider a reduced (open) version of the original circulation model in which we remove the equations for all the variables that are already described by the 3D counterpart. The equations of the open system are reported in Appendix A. By denoting with \mathbf{Q}^{0D} and \mathbf{p}^{0D} the vectors containing flowrates and pressures of the 0D model, respectively, we refer to the open system with the notation

$$\mathcal{C}(\mathbf{Q}^{\text{0D}}, \mathbf{p}^{\text{0D}}) = 0.$$

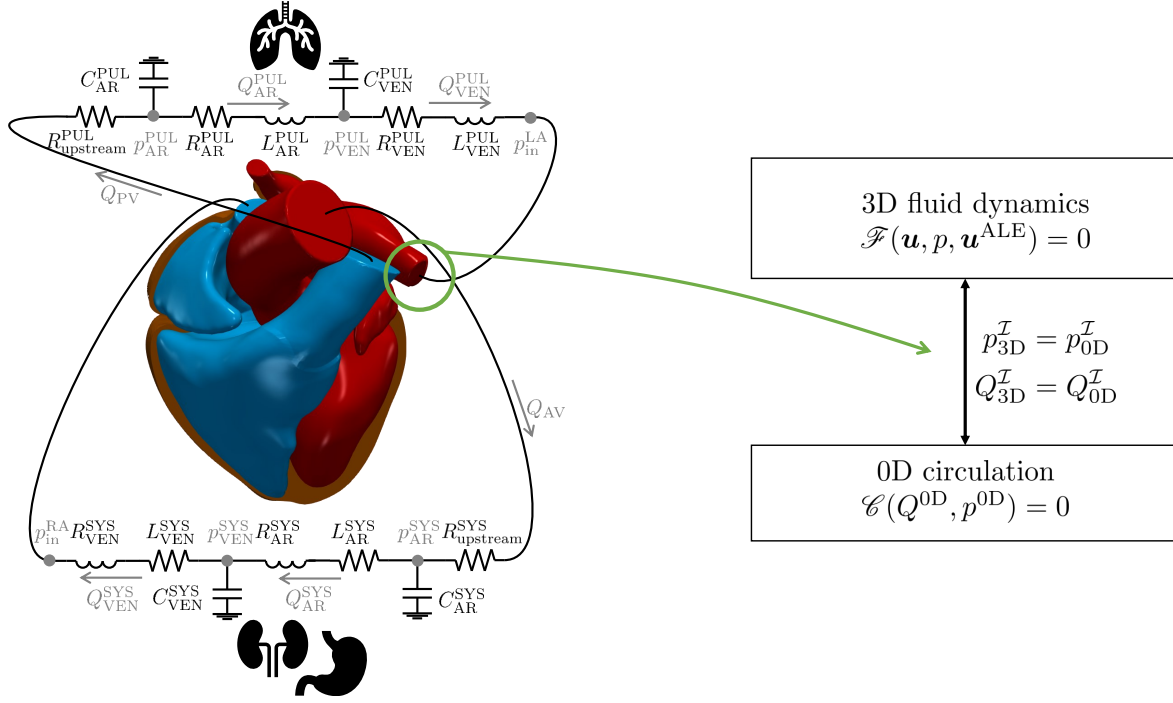


Figure 3: The 3D-0D fluid dynamics model of the whole-heart coupled to the surrounding circulation.

The coupling between the 3D CFD model and the open 0D model consists in the enforcement of the continuity of pressures and flowrates on the artificially chopped boundaries $\Gamma^{\mathcal{I}}$ of the fluid domain, yielding the following conditions:

$$\begin{cases} p_{3D}^{\mathcal{I}} = p_{0D}^{\mathcal{I}} & \text{on } \Gamma^{\mathcal{I}} \times (0, T), \\ Q_{3D}^{\mathcal{I}} = Q_{0D}^{\mathcal{I}} & \text{on } \Gamma^{\mathcal{I}} \times (0, T), \end{cases} \quad (4a)$$

$$\quad (4b)$$

which express dynamic and kinematic coupling, respectively, with¹

$$p_{3D}^{\mathcal{I}} = \frac{1}{|\Gamma^{\mathcal{I}}|} \int_{\Gamma^{\mathcal{I}}} p, \quad Q_{3D}^{\mathcal{I}} = \int_{\Gamma^{\mathcal{I}}} (\mathbf{u} - \mathbf{u}^{\text{ALE}}) \cdot \mathbf{n}. \quad (5)$$

Considering the whole-heart fluid domain (see Figure 2b), the interface boundaries are $\Gamma^{\mathcal{I}} = \Gamma^{\text{in,RH}} \cup \Gamma^{\text{out,RH}} \cup \Gamma^{\text{in,LH}} \cup \Gamma^{\text{out,LH}}$. The 0D pressures ($p_{0D}^{\mathcal{I}}$) and flowrates ($Q_{0D}^{\mathcal{I}}$) are [48, 100]:

$$\begin{aligned} p_{0D}^{\text{in,RH}} &= p_{\text{RA}}^{\text{in}}, & Q_{0D}^{\text{in,RH}} &= -Q_{\text{VEN}}^{\text{SYS}}, \\ p_{0D}^{\text{out,RH}} &= p_{\text{AR}}^{\text{PUL}} + R_{\text{upstream}}^{\text{PUL}} Q_{\text{PV}}, & Q_{0D}^{\text{out,RH}} &= Q_{\text{PV}}, \\ p_{0D}^{\text{in,LH}} &= p_{\text{LA}}^{\text{in}}, & Q_{0D}^{\text{in,LH}} &= -Q_{\text{VEN}}^{\text{PUL}}, \\ p_{0D}^{\text{out,LH}} &= p_{\text{AR}}^{\text{SYS}} + R_{\text{upstream}}^{\text{SYS}} Q_{\text{AV}}, & Q_{0D}^{\text{out,LH}} &= Q_{\text{AV}}. \end{aligned}$$

From the point of view of the 3D CFD model, the conditions expressed by Equation (5) are defective, since they prescribe the average pressure and the total flow rate over the entire section $\Gamma^{\mathcal{I}}$, rather than pointwise stress and velocity distributions [56]. We choose to complete the pressure condition as

$$\sigma(\mathbf{u}, p)\mathbf{n} = -p^{\mathcal{I}}\mathbf{n}, \text{ on } \Gamma^{\mathcal{I}} \times (0, T). \quad (6)$$

The flowrate condition, conversely, is left in its defective form, since it is sufficient for the algorithm we use for the 3D-0D coupling (see Section 3).

¹We define the sign of the flowrate in accordance with the outward unit normal \mathbf{n} . Thus, an inlet flowrate (entering velocity) will be, by definition, negative.

Algorithm 1 Numerical scheme for the EM-driven CFD simulation of the whole heart

Solve whole-heart EM model
Pick solution in the last heartbeat: $\rightarrow \mathbf{d}_i^{\text{EM}}$, for $i = 0, \dots, N$
Restrict \mathbf{d}_i^{EM} on $\partial\Omega_i^{\text{S,endo}}$: $\mathbf{d}_i^{\partial\Omega}$, for $i = 0, \dots, N$
Solve fluid domain displacement problem: $\mathcal{D}(\mathbf{d}_i, \mathbf{d}_i^{\partial\Omega}) = 0$, for $i = 0, \dots, N$
Build approximant: $\tilde{\mathbf{d}}(t)$
Initialization: $n = 0$, $\mathbf{u}_0 = \mathbf{0}$
while $n < N_t$ **do**
 Update valves leaflet position
 Compute ALE velocity: $\mathbf{u}_{n+1}^{\text{ALE}} = \frac{\tilde{\mathbf{d}}_{n+1} - \tilde{\mathbf{d}}_n}{\Delta t}$.
 Solve circulation: $\mathcal{C}(\mathbf{Q}_{n+1}^{\text{OD}}, \mathbf{p}_{n+1}^{\text{OD}}) = 0$ with data $Q_{\text{OD},n}^{\mathcal{I}}$
 Compute interface data (0D \rightarrow 3D): $p_{\text{OD},n+1}^{\mathcal{I}} \rightarrow p_{\text{3D},n+1}^{\mathcal{I}}$
 Solve fluid dynamics: $\mathcal{F}(\mathbf{u}_{n+1}, p_{n+1}, \mathbf{u}_{n+1}^{\text{ALE}}) = 0$, with Neumann data $p_{\text{3D},n+1}^{\mathcal{I}}$
 Compute interface data (3D \rightarrow 0D): $Q_{\text{3D},n+1}^{\mathcal{I}} \rightarrow Q_{\text{OD},n+1}^{\mathcal{I}}$
 $n \leftarrow n + 1$.
end while

3. Numerical methods

In this section, we describe the numerical methods we use to solve our multiphysics and multiscale system. The overall algorithm is presented in Algorithm 1 and graphically represented in Figure 4. We can subdivide the overall procedure in a preliminary phase, in which we solve the EM simulation [64] and the fluid domain displacement problem to lift the boundary displacement to the fluid bulk domain, followed by the coupled 3D-0D CFD simulation.

Numerical methods for the EM model. For the numerical approximation of the whole-heart EM model we employ the efficient Segregated-Staggered scheme [65, 83, 64]. In this numerical scheme, the different cardiac physical models, contributing to both the 3D EM and the 0D blood circulation, are sequentially solved in a segregated manner, using different resolutions in space and time to properly account for the heterogeneous space and time scales characterizing different physical processes [101].

For the space discretization, we use the Finite Element (FE) method with continuous FE on a tetrahedral mesh. We consider FE of order 2 (\mathbb{P}_2) for the electrophysiology to capture the traveling wave dynamics and FE of order 1 (\mathbb{P}_1) for both the activation and the mechanics [64].

For the time discretization, we use finite difference schemes [102]. Specifically, cardiac electrophysiology is solved with Backward Differentiation Formula (BDF) of order 2, using an Implicit-Explicit (IMEX) scheme where the diffusion term is treated implicitly, the ionic and reaction terms explicitly. The ionic variables are advanced in time through an IMEX scheme [65, 83, 64]. We solve the active contraction problem with an IMEX BDF1 method, and the mechanical problem with a fully-implicit BDF1 scheme [83]. Finally, an IMEX scheme of the first order is used for the circulation [64]. Moreover, two different time steps are used: a finer one for the electrophysiology and a larger one for both the activation, the mechanics and the circulation [65]. Finally, we employ recently developed stabilization methods – related to the circulation and the fibers-stretch-rate feedback – that are crucial to obtain a stable solution in a four-chamber simulation scenario [103, 104]. Concerning the linear systems arising from the discretization of the whole-heart EM problem we use: the conjugate gradient for the electrophysiology and the GMRES method for both the mechanics and the activation, both empowered by an algebraic multigrid (AMG) preconditioner. Finally, we solve the non-linear saddle-point problem arising from the coupling between the mechanics and the circulation by means of a Newton algorithm using, at the algebraic level, the Schur complement reduction [83, 65].

For further details about the numerical methods we use in the whole-heart EM model, we refer to [65, 83, 64].

Numerical methods for the fluid domain displacement problem. After simulating the whole-heart EM and reaching a limit cycle in terms of pressure and volumes, we extract the solution from the last simulated heartbeat. We restrict this solution to the heart endocardium and the endothelium of outflow tracts, obtaining $N + 1$ solutions defined on the boundary of the fluid domain ($\mathbf{d}_i^{\partial\Omega}$, with $i = 0, \dots, N$). We project $\mathbf{d}_i^{\partial\Omega}$ onto the CFD mesh with piecewise linear interpolation, then solve the fluid domain displacement problem in Equation (1) to obtain the ALE displacement \mathbf{d} . We discretize the lifting problem in Equation (1) using FEs of order 1 (\mathbb{P}_1) and the linear system

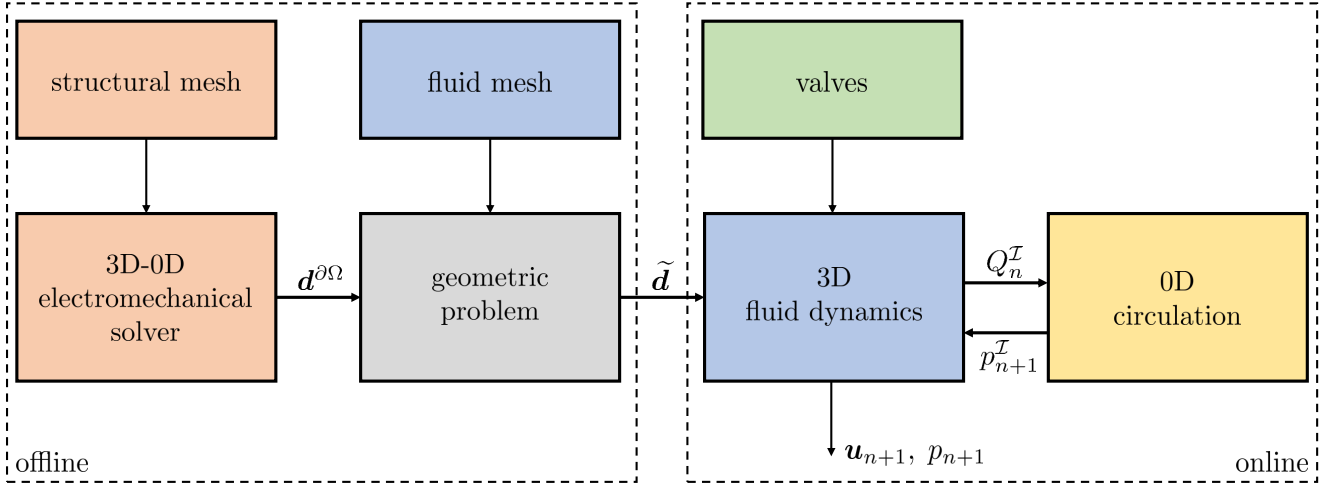


Figure 4: Graphical representation of the overall algorithm to simulate the whole-heart hemodynamics driven by the EM model.

arising from its discretization is preconditioned with an AMG preconditioner. We solve the resulting linear system with the conjugate gradient method. The smoothing spline approximation is computed independently for each mesh node, and the approximant is constructed following the optimization procedure described in [105]. To compute the ALE velocity, we use BDF1 to discretize in time Equation (2).

Numerical methods for the CFD cardiac model. We discretize Equation (3) in space using FEs of order 1 for both velocity and pressure ($\mathbb{P}_1 - \mathbb{P}_1$). We employ the Variational Multiscale - Large Eddy Simulation (VMS-LES) method to obtain a stable formulation of the NS-ALE-RIIS equations discretized via equal order FE spaces. This also allows us to control instabilities arising from the advection-dominated regime, and to model transition-to-turbulence in the LES framework [106, 107, 16]. The VMS-LES formulation accounts for the ALE framework and the RIIS modeling used for valves. For the complete formulation, we refer to [27].

For the time discretization, we consider a uniform partition of the temporal domain in N_t subintervals (t_n, t_{n+1}) of uniform size Δt , with $n = 0, \dots, N_t - 1$. We denote from here quantities approximated at time t_n with the subscript n , e.g. $\mathbf{u}_n \approx \mathbf{u}(t_n)$. We advance the problem in time by means of BDF1. To reduce the computational burden of the numerical simulations, we use a semi-implicit treatment of the nonlinearities, as done in [106]. The overall numerical scheme for the fluid dynamics problem is detailed in [27].

Since Neumann boundary conditions may give rise to instability phenomena in case of inflow, we set backflow stabilization on all the Neumann boundaries in the inertial form presented in [108].

The linear system arising from the discretization of Equation (3) is preconditioned with the aSIMPLE preconditioner [109], and each of its blocks is preconditioned with an AMG preconditioner. The linear system is then solved at each time step by the GMRES method.

Numerical method for the 0D circulation model. We solve the system of ODEs of the circulation problem with an IMEX method of the first order. The time-step size Δt employed for its numerical discretization is the same used for the BDF advancing scheme in the 3D problem.

Numerical scheme for the coupled CFD problem. After initialization, for each temporal step of the CFD problem, we update the position of valve leaflets and we compute the ALE velocity. At every time step, we solve the 3D and 0D subproblems independently. First, we solve the 0D open circulation problem using Q_n^I as input (i.e. the flowrates computed in the 3D model at previous timestep, namely $Q_{\text{VEN},n}^{\text{SYS}}, Q_{\text{PV},n}, Q_{\text{VEN},n}^{\text{PUL}}, Q_{\text{AV},n}$). Then, from the solution of the circulation, we compute the pressures p_{n+1}^I at the interfaces and solve the fluid dynamics problem providing those pressures as Neumann boundary conditions at inlet and outlet sections. Finally, we compute the interface data from the 3D to the 0D model, i.e. Q_{n+1}^I . This approach treats the coupling between the 3D and 0D subproblems in a segregated and explicit way.

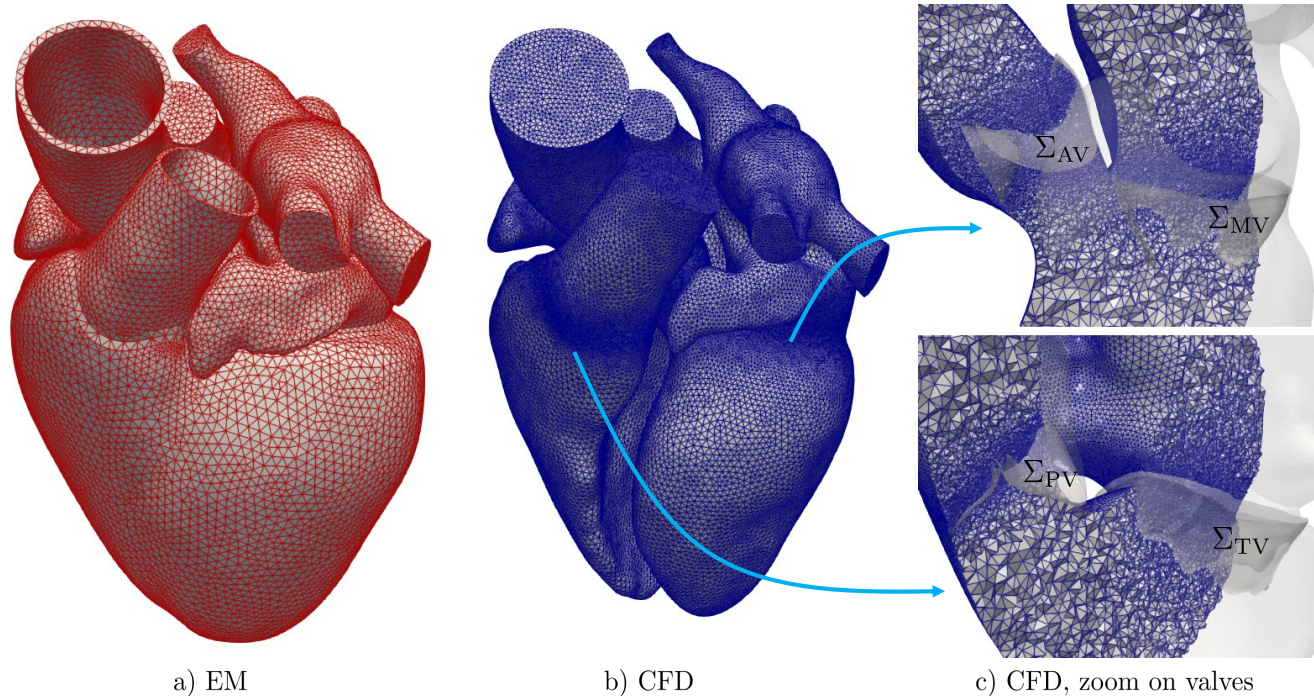


Figure 5: Tetrahedral meshes used in the computational model: a) mesh for the EM simulation, b) mesh for the CFD simulation, c) mesh refinement on the valves region of the CFD mesh.

| Simulation | Mesh size [mm] | | | Cells | Points | Physics | DOFs | Δt [s] |
|------------|----------------|------|------|-----------|---------|-------------------|-----------|-------------------|
| | min | avg | max | | | | | |
| EM | 0.860 | 2.97 | 5.34 | 180 472 | 46 915 | Electrophysiology | 310 505 | $5 \cdot 10^{-5}$ |
| | | | | | | Mechanics | 140 745 | 10^{-3} |
| | | | | | | Circulation | - | 10^{-3} |
| CFD | 0.210 | 1.04 | 3.82 | 3 892 584 | 652 204 | Fluid dynamics | 2 608 816 | 10^{-4} |
| | | | | | | Circulation | - | 10^{-4} |

Table 1: Setup of whole-heart EM and CFD simulations (mesh details and time step sizes).

4. Numerical results

In this section, we present the numerical results using the whole-heart fluid dynamics model. In Section 4.1, we introduce the computational setting of the whole-heart EM and CFD simulations. Section 4.2 is devoted to the manual calibration of the RDQ20 active contraction model to produce physiological flowrates in the EM simulation. The physiological results of the overall computational model are presented in Section 4.3. Finally, we apply the multiphysics computational model to the pathological case of LBBB in Section 4.4.

4.1. Computational setup

We consider a realistic whole-heart geometry provided by the Zygote solid 3D heart model [110], an anatomically CAD model representing an average healthy human heart reconstructed from high-resolution computer tomography scan data. We generate whole-heart tetrahedral meshes for the EM and CFD problems that we report in Figure 5. Meshes are generated with `vtk` [111] using the methods and tools discussed in [112, 64, 27]. Details on the meshes for the EM and CFD simulations are provided in Table 1. The valve leaflets are thin structures that we characterize, in the context of the RIIS method, by small values of ε_k . To correctly capture the immersed surfaces, we refine the CFD mesh close to the valve regions, as shown in Figure 5c. Specifically, following [77], we choose h_k such that $\varepsilon_k \geq 1.5h_k$, where h_k is the minimum mesh size of the fluid mesh in the valve region.

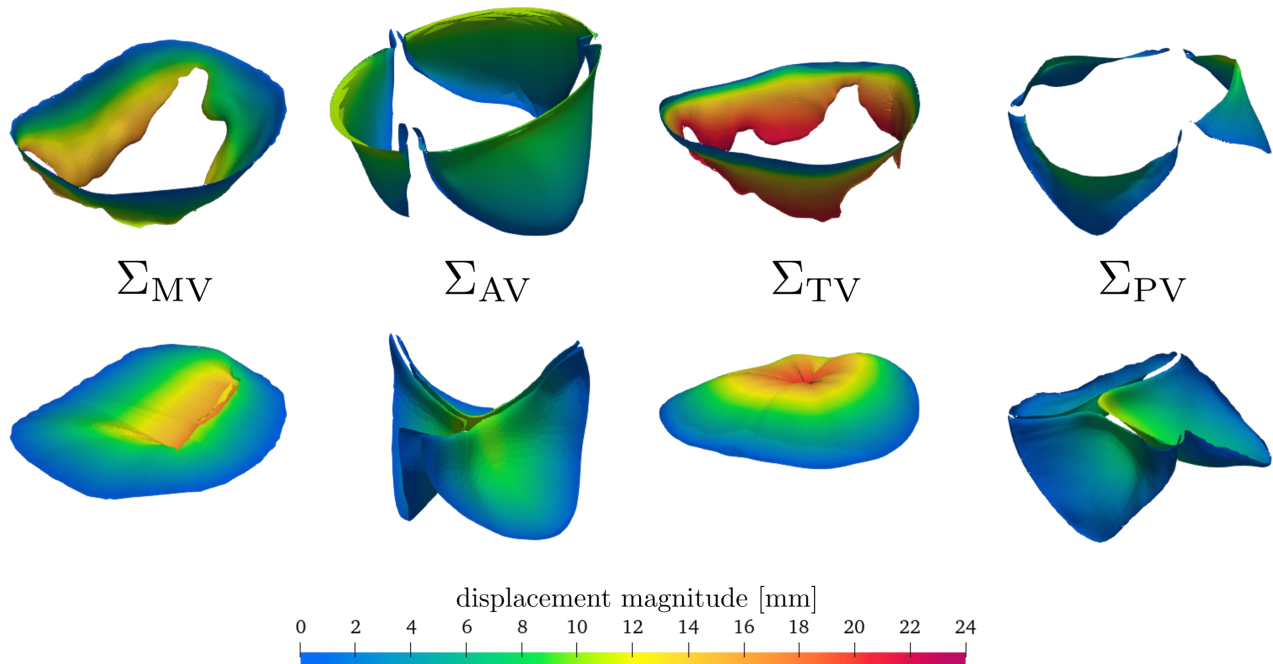


Figure 6: Cardiac valves in their open and closed configurations coloured according to displacement magnitude. Valves geometry are provided by Zygote [110], and we define displacement field aimed at closing and opening the leaflets.

We carry out EM and CFD simulations in `lifex` [113, 114, 115, 116]², a high-performance C++ FE library developed within the `iHEART` project³, mainly focused on cardiac simulations and based on the `deal.II` finite element core [117, 118, 119].

Numerical simulations are run in parallel on the GALILEO100 supercomputer⁴ at the CINECA supercomputing center, using 240 and 480 cores for the EM and CFD simulations, respectively. The computational time to carry out a single heartbeat is about 1 hour and 20 minutes for the EM simulation and 56 hours for the CFD simulation.

For the parameters of the EM model, we use the same values as in [64] with some minor differences reported in Appendix B. As we better discuss in Section 4.2, a huge difference in terms of setup of the EM simulation between [64] and the present work consists in the manual calibration of the active contraction model to compute physiological blood flowrates. We simulate 20 heartbeats of the whole-heart EM, and we report numerical results related to the last heartbeat, after verifying that the solution is sufficiently close to a periodic limit cycle (in terms of pressure and volume transients). We consider an heartbeat period of $T_{\text{HB}} = 0.8$ s. We pick the last simulated EM heartbeat as input displacement for the CFD simulation. We set as initial condition for the velocity $\mathbf{u}_0 = \mathbf{0}$. The initial state of the circulation model (for the coupling with the fluid dynamics) is taken equal to the values reached at the beginning of the last heartbeat in the EM simulation. Moreover, as detailed in Appendix B, all the values of the parameters involved in the circulation model are the same for the EM and the fluid dynamics simulations. The physical parameters for blood are density $\rho = 1.06 \cdot 10^3$ kg/m³ and dynamic viscosity $\mu = 3.5 \cdot 10^{-3}$ kg/(m.s). We simulate two heart cycles, and we report the solution on the second cycle to remove the consequences of an unphysical null initial condition. For the numerical results visualization (for both EM and CFD), we shift the time domain in $(0, T_{\text{HB}})$.

The Zygote cardiac valves [110] are provided in their open configuration (TV, MV) and closed configuration (PV, AV). Thus, we define displacement fields aimed at closing and opening their leaflets, based on signed-distance functions and the solution of Laplace-Beltrami problems [112, 27]. In Figure 6, we report the valves in their open

²<https://lifex.gitlab.io/>

³iHEART - An Integrated Heart model for the simulation of the cardiac function, European Research Council (ERC) grant agreement No 740132, P.I. A. Quarteroni, 2017-2023

⁴528 computing nodes each 2 x CPU Intel CascadeLake 8260, with 24 cores each, 2.4 GHz, 384GB RAM. See <https://wiki.u-gov.it/confluence/display/SCAIUS/UG3.3%3A+GALILEO100+UserGuide> for technical specifications.

| | | MV | AV | TV | PV |
|-----------------|----------|-----------|-----------|-----------|-----------|
| opening time | [s] | 0.710 | 0.262 | 0.700 | 0.279 |
| closing time | [s] | 0.208 | 0.666 | 0.194 | 0.677 |
| R_k | [kg/m/s] | 10^4 | 10^4 | 10^4 | 10^4 |
| ε_k | [mm] | 0.68 | 0.67 | 0.77 | 0.52 |

Table 2: Setup of the RIIS method to model cardiac valves.

and closed configurations, colored according to the leaflets’ displacement magnitude. We open and close the valves instantaneously (i.e. in one time step) at the times reported in Table 2. These times are chosen by selecting the initial and final times of the isovolumetric phases. The values we choose for ε_k , reported in Table 2, allow to have a physiological representation of the valve leaflet. Indeed, we choose ε_k by averaging the values of the leaflet thicknesses reported in [120]. Furthermore, the valve resistances values R_k are reported in Table 2. We found that the condition number of the linear system associated to the FE discretization of the fluid dynamics problem becomes larger as the ratio R_k/ε_k increases. Thus, to keep contained the computational cost of the CFD simulation, we choose as R_k the minimum value that guarantees impervious valves.

4.2. Calibration of the RDQ20 active contraction model to achieve physiological flows

Among the different components at the basis of cardiac EM simulations, the model describing the force generation at the microscale plays a pivotal role. Indeed, not only the amount of force the muscle develops depends on it, but also its temporal distribution over the heartbeat, i.e. the kinetics of contraction and relaxation. As demonstrated in [64], a biophysically detailed force generation model can effectively reproduce flowrates through the semilunar valves, which are very often severely overestimated in models involving less detailed active contraction models [121, 122]. Since the electromechanical displacement drives the fluid dynamics model, the CFD flow rates are the same as those of the electromechanical simulation, and are therefore heavily affected by the choice of the force generation model. Thus, special care must be devoted to the choice and calibration of the active contraction model.

For the above reasons, we chose to use the RDQ20 model [81], that is an active force model with high biophysical fidelity and that is able to reproduce the main features of the experimentally observed behaviors. The RDQ20 model is based on a detailed description of the calcium-driven regulation of the thin filament, with explicit representation of end-to-end cooperative interactions, and a description of the attachment-detachment process of crossbridges, at the basis of the force-velocity relationship. Thereby, the model is able to reproduce the main mechanisms of contractility regulation, mediated by calcium, fiber strain and fiber strain-rate. In particular, the fiber strain-rate feedback, which is responsible for the well-known force-velocity relationship, plays a central role in the regulation of hemodynamic flows, as demonstrated in [64] and confirmed in the present study.

On this basis, we refine the calibration of the RDQ20 model, with a particular care on fluxes through semilunar valves obtained by means of the 0D model in the EM simulation. We employ as a starting point the calibration used in [64], suitable for the coupling with the TTP06 ionic model [88] (see Table 3, setting A). In this paper, we focus on the calibration of the ventricles only, whereas for the atria, we employed the same parameters of the RDQ20 model used in [64]. In Table 4, column A, we report a list of biomarkers obtained by using the calibration A in the EM simulation. To better appreciate the effect of each calibration on different biomarkers, we provide a graphical representation in Figure 9. We normalize each biomarker in the interval $[-1, 1]$ using reference physiological values from the literature and reported in Table 4. Although the biomarkers characterizing the overall cardiac function (i.e. end-systolic and end-diastolic volume, stroke volume and ejection fraction) are within reference ranges, the maximum blood flux across valves is significantly above the physiological range. In other terms, even if the total ejected blood is physiological, the instantaneous flow peak is too large. This would clearly have a strong negative impact on the results of fluid dynamics simulations. For instance, an excessively high velocity through the valve may result in high pressure gradients, and an overall incorrect stress distribution over valve leaflets and cardiac walls [123, 124].

To address this issue, we slow down the process of force generation, so that the tissue contractility is developed at a lower rate. More precisely, we reduce the association-dissociation rates of troponin and tropomyosin of the RDQ20 model (i.e. K_{off} and K_{basic}) by a factor 2. Moreover, to compensate for the lower peak force caused by a slower kinetics, we increase the crossbridge level contractility (i.e. α_{XB}). We consider three different levels of contractility, as reported in Table 3, respectively in columns B, C and D. However, as we show in Table 4 and Figure 7, on the one hand, we achieve the desired effect of reducing semilunar peak flows, thus bringing them within the expected ranges. On the other hand, we compute significantly reduced stroke volume and ejection fraction for both chambers, thus

| Parameter | | A | B | C | D | E |
|--|-------------------------------|---------|-------------------|-------------------|-------------------|-------------------|
| Regulatory units dynamics | | | | | | |
| Q | [-] | 2 | 2 | 2 | 2 | 2 |
| \bar{k}_d | [μM] | 0.36 | 0.36 | 0.36 | 0.36 | 0.36 |
| α_{k_d} | [$\mu\text{M}/\mu\text{m}$] | -0.2083 | -0.2083 | -0.2083 | -0.2083 | -0.2083 |
| μ | [-] | 10 | 10 | 10 | 10 | 10 |
| γ | [-] | 30 | 30 | 30 | 30 | 30 |
| K_{off} | [1/s] | 8 | (*) 4 | (*) 4 | (*) 4 | (*) 4 |
| K_{basic} | [1/s] | 4 | (*) 2 | (*) 2 | (*) 2 | (*) 2 |
| Crossbridge dynamics (prescribed) | | | | | | |
| v_0 | [1/s] | 2 | 2 | 2 | 2 | (*) 0.5 |
| v_{max} | [1/s] | 8 | 8 | 8 | 8 | (*) 2 |
| \bar{k}_2 | [-] | 66 | 66 | 66 | 66 | 66 |
| μ_0^{iso} | [-] | 0.22 | 0.22 | 0.22 | 0.22 | 0.22 |
| Crossbridge dynamics (automatically calibrated) | | | | | | |
| r_0 | [1/s] | 134.31 | 134.31 | 134.31 | 134.31 | 33.24 |
| α | [-] | 25.184 | 25.184 | 25.184 | 25.184 | 24.93 |
| $\mu_{f_P}^0$ | [1/s] | 32.225 | 32.225 | 32.225 | 32.225 | 7.98 |
| $\mu_{f_P}^1$ | [1/s] | 0.768 | 0.768 | 0.768 | 0.768 | 0.192 |
| Micro-macro upscaling | | | | | | |
| a_{XB} | [MPa] | 1500.0 | (*) 1550.0 | (*) 2925.0 | (*) 5214.5 | (*) 1550.0 |

Table 3: Different calibrations of the RDQ20 active contraction model: A) calibration from [64]; B) C) D) Reduced K_{off} , K_{basic} and different levels of a_{XB} ; E) Reduced v_0 , v_{max} . Parameters that are modified with respect to A are highlighted by the symbol (*). We remark that the parameters r_0 , α , $\mu_{f_P}^0$ and $\mu_{f_P}^1$ are automatically calibrated from the four quantities v_0 , v_{max} , \bar{k}_2 and μ_0^{iso} (for further details, see [81]); therefore, the symbol (*) is not reported for these four parameters. For the description of each parameter, we refer to the original paper of the RDQ20 model [81].

| Biomarker | | Physiological values | | A | B | C | D | E |
|--------------------------------|--------|----------------------|--------|----------------------------|------------------------------|------------------------------|------------------------------|------|
| ESV _{LV} | [mL] | 35 to 80 | [125] | 53.8 | 66.7 | 53.5 | 45.9 | 66.4 |
| ESV _{RV} | [mL] | 69 \pm 22 | [126] | 58.0 | 79.8 | 65.3 | 56.0 | 72.3 |
| EDV _{LV} | [mL] | 126 to 208 | [125] | 150 | 128 | (\downarrow) 108 | (\downarrow) 87.9 | 151 |
| EDV _{RV} | [mL] | 144 \pm 23 | [127] | 153 | 152 | 134 | 119 | 159 |
| SV _{LV} | [mL] | 81 to 137 | [125] | 96.3 | (\downarrow) 61.5 | (\downarrow) 54.9 | (\downarrow) 42.0 | 84.9 |
| SV _{RV} | [mL] | 94 \pm 15 | [127] | 95.4 | (\downarrow) 72.3 | (\downarrow) 69.1 | (\downarrow) 63.2 | 87.1 |
| EF _{LV} | [%] | 49 to 73 | [128] | 64.2 | (\downarrow) 48.0 | 50.2 | (\downarrow) 47.8 | 56.1 |
| EF _{RV} | [%] | 53 \pm 6 | [129] | (\uparrow) 62.2 | 47.5 | 51.4 | 53.0 | 54.6 |
| Q _{AV} ^{max} | [mL/s] | 427 \pm 129 | [130] | (\uparrow) 697 | 327 | 347 | 304 | 399 |
| Q _{PV} ^{max} | [mL/s] | 427 \pm 129 | [130]† | (\uparrow) 756 | 397 | 427 | 443 | 478 |
| P _{LV} ^{max} | [mmHg] | 119 \pm 13 | [131] | (\uparrow) 154 | (\downarrow) 99.5 | (\downarrow) 93.2 | (\downarrow) 80.7 | 120 |
| P _{RV} ^{max} | [mmHg] | 35 \pm 11 | [132] | 37.2 | 34.9 | 38.2 | 41.6 | 32.2 |

Table 4: Effects of different calibrations of the RDQ20 active contraction model on mechanics and hemodynamics biomarkers. Biomarkers highlighted by the symbols (\uparrow) and (\downarrow) lie outside the reference ranges, denoting values too large or too small, respectively, compared with reference ranges. †: for the maximum PV flowrate, in absence of clinical ranges from literature, we consider the same normal values of the AV flowrate. Each column corresponds to a different calibration as detailed in Table 3.

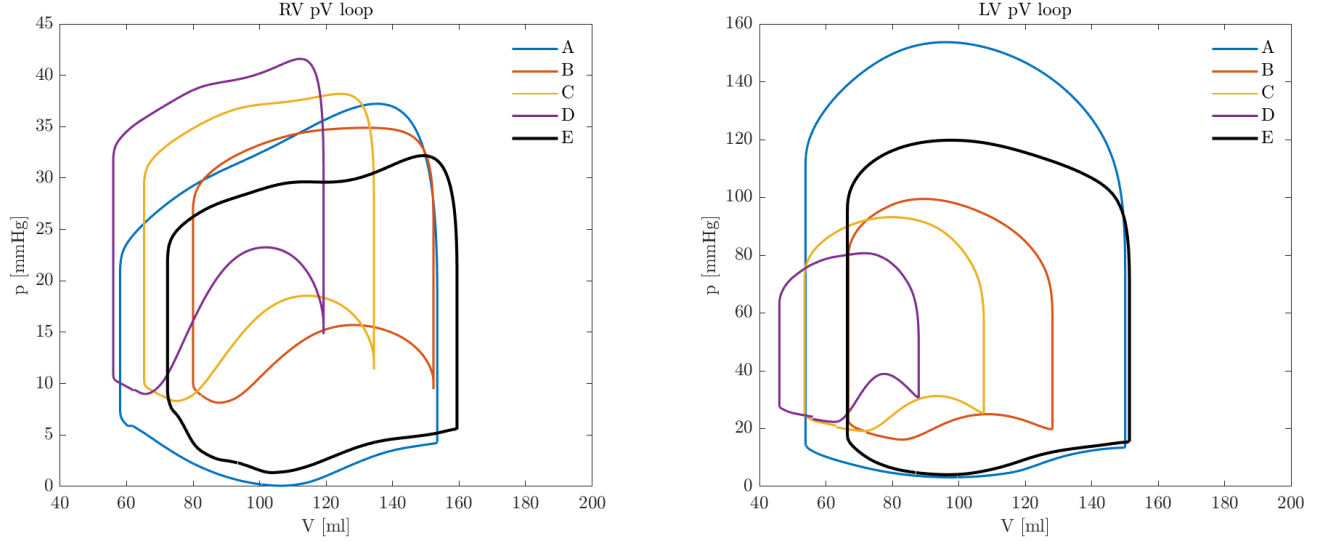


Figure 7: pV loops of RV and LV obtained with different calibrations of the RDQ20 active contraction model. Each line corresponds to a different calibration as detailed in Table 3.

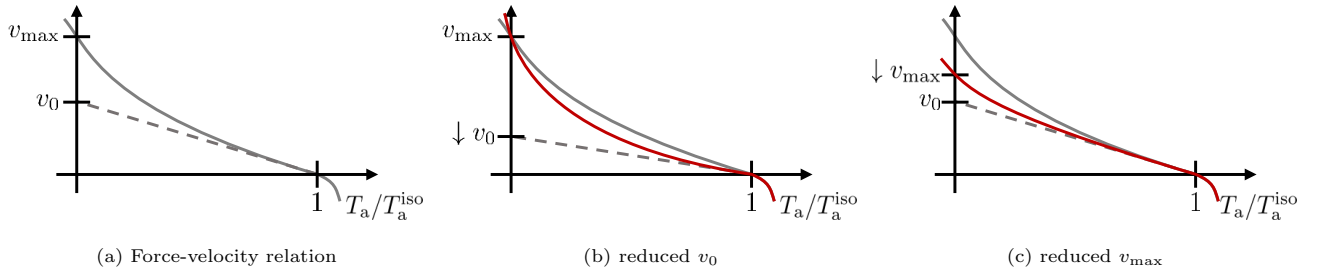


Figure 8: Representation of the well-known force-velocity relationship of muscle cells. The normalized active tension T_a/T_a^{iso} , where T_a^{iso} denotes the force in isometric conditions, is a decreasing function of the shortening velocity v . As shown in the figure, v_{max} is the shortening velocity for which the active tension reaches zero, while v_0 is the slope of the curve in correspondence of the isometric conditions (i.e. $v = 0$). (a) generic force-velocity relationship, (b) effect of reducing v_0 (in grey, the curve from (a)), (c) effect of reducing v_{max} (in grey, the curve from (a)).

moving out of physiological ranges. Notice also that this issue is also not resolved by adjusting the contractility. In fact, by raising a_{XB} , not only the state of contractility in systole is changed, but also in diastole, leading to a reduced end-diastolic volume and, therefore, nullifying the effect of increased contractility, due to the Frank-Starling mechanism. The three cases shown in Table 4 (B, C and D) are three illustrative cases out of the many that we tested, but without being able to reduce peak flows within the expected ranges while maintaining a physiological ejection fraction. The tests evidenced a paradigmatic short-blanket problem, whereby just acting on kinetics and contractility it is not possible to lower the flows while maintaining a regular ejection fraction. Evidently, another element must be taken into account.

Based on the results of [64], which showed that, by neglecting the fibers-stretch-rate feedback, blood flows through the semilunar valves are significantly overestimated, we modified the calibration so as to, on the contrary, strengthen the effect of this feedback, but without changing either the isometric force or the kinetics. Specifically, we acted in such a way as to steepen the force-velocity relationship, the microscopic mechanism underlying the fibers-stretch-rate feedback, by modifying the parameters governing cross-bridge dynamics. For this purpose, we took advantage of the calibration technique illustrated in [81], by which the RDQ20 model can be tuned to achieve a desired force-velocity relationship. Two features of the force-velocity relationship can be selected, namely the maximum shortening velocity (v_{max}), that is the velocity corresponding to vanishing active force, and the tangent to the curve under isometric conditions (v_0). The geometric meaning of the two quantities is illustrated in Figure 8.

Hence, starting from the B calibration, we modified the parameters to obtain a v_{max} and a v_0 equal to one-fourth of the original ones (see Table 3, column E). As evidenced in Table 4, with the setting E all biomarkers fall within physiological ranges (see also Figure 7). We believe that this result can be explained precisely by the mechanism

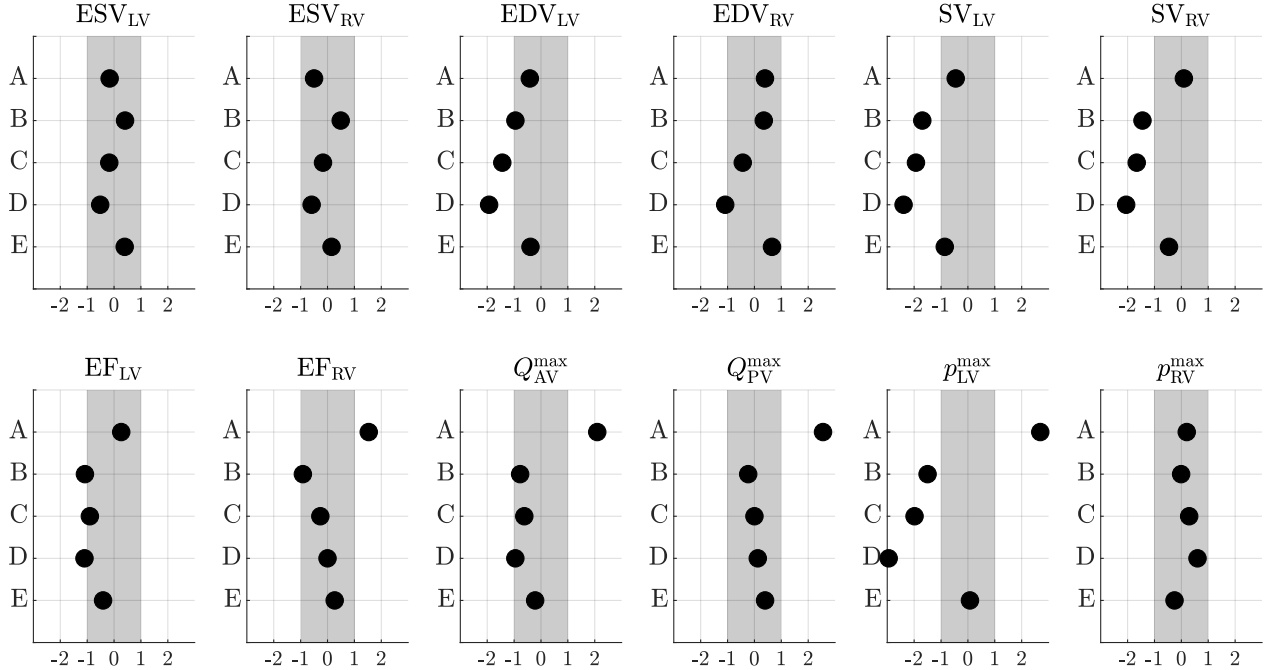


Figure 9: Effects of different calibrations of the RDQ20 active contraction model on mechanics and hemodynamics biomarkers. Each biomarker has been normalized according to the reference ranges provided in Table 4 in the interval $[-1, 1]$. The gray rectangle denotes the reference range, whereas each black dots indicate the result of the EM simulation with a different calibration of the RDQ20 model, as detailed in Table 3.

of fibers-stretch-rate feedback, whereby regions of the tissue undergoing rapid shortening experience a decrease in developed force, thus promoting a more homogeneous shortening in space and without significant spikes in time, with a resulting viscous-like effect. In conclusion, blood flow is redistributed more evenly over the duration of the ejection phase.

Based on the very good match with the reference values of the different biomarkers, in this work we use the calibration E as the baseline for EM simulations.

4.3. Heart physiology and validation against clinical biomarkers

Figure 10 shows the whole-heart EM displacement for a single, representative heartbeat, where we highlight six different phases: isovolumetric contraction, ejection (peak and mid-deceleration), isovolumetric relaxation, ventricular passive filling, and atrial contraction. As pointed out in [64], the whole-heart EM model can correctly reproduce the cardiac physiological motion. Moreover, as shown in Section 4.2, we found that, after a thorough calibration of the active contraction model, our numerical results are consistent with normal values found in literature in terms of several volumetric biomarkers.

In Figure 11, we report the volumes of the heart chambers and large arteries versus time, and we highlight time instants in which valves open and close. In Figure 15, we report the volume rendering of the velocity magnitude obtained with our EM-driven CFD simulation. We start our fluid dynamics simulation at the end of ventricular diastole.

During the active atrial contraction (Figure 15a), we observe the blood flowing from atria to ventricles, producing two high-speed jets in the MV and TV. This moment corresponds to the A-wave, as shown in Figure 14. In order to assess whether our numerical simulation is correctly reproducing the physiological heart function, we compare the peak velocities through valves with physiological ranges available in literature and acquired in healthy subjects. We report this comparison in Table 5. During diastole, we obtain lower velocities in the TV compared to MV, consistently with clinical measurements available in literature [133, 44].

During the isovolumetric contraction (Figure 15b), all valves are closed and the ventricular volumes remain constant. We measure lower velocity values compared to filling and ejection phases. Moreover, we found that the intraventricular pressure is not well defined and is prone to oscillations. As a matter of fact, since we are using EM as unidirectional input of the CFD model, the dynamic balance between hemodynamics and tissue

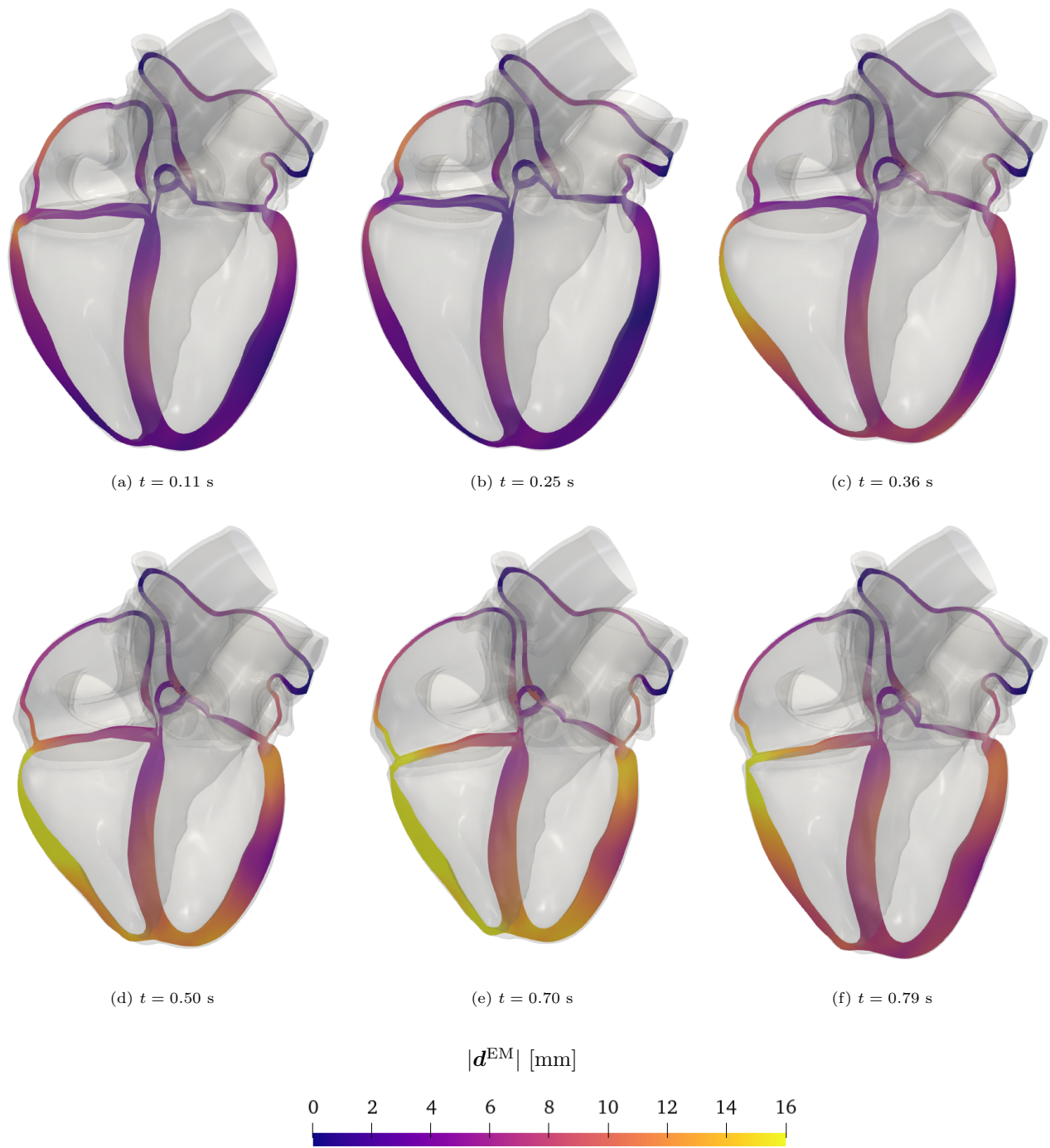


Figure 10: Whole heart deformed with EM displacement (with respect to the reference stress-free configuration) and colored according to its magnitude for a single, representative heartbeat: (a) active atrial contraction, (b) isovolumetric contraction, (c) ejection (peak), (d) ejection (mid-deceleration), (e) isovolumetric relaxation, (f) passive ventricular filling.

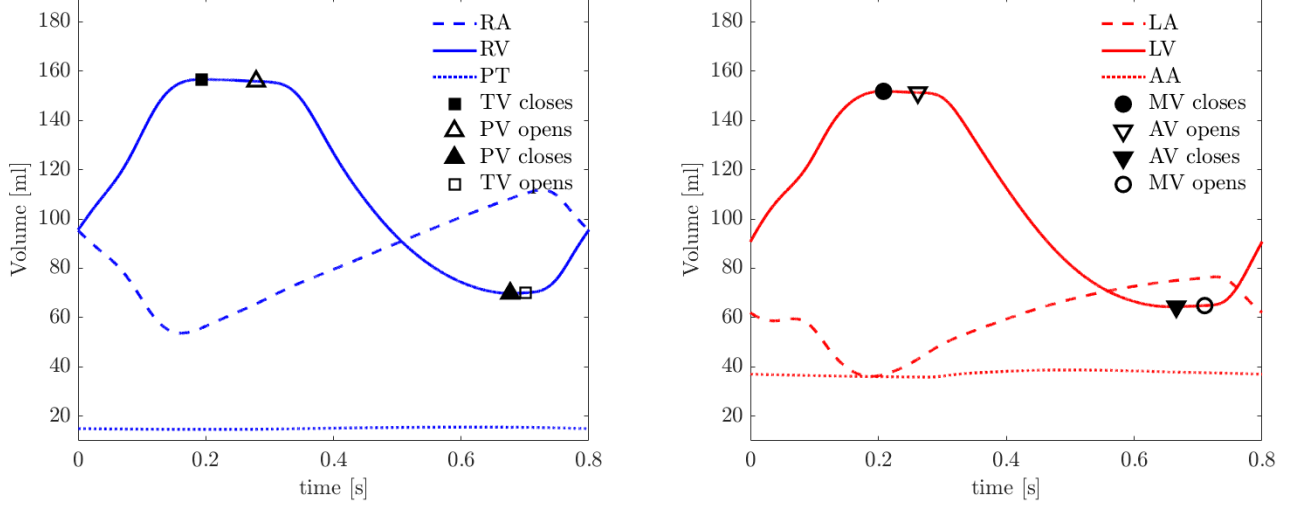


Figure 11: Volumes of RA, RV, PT (left) and LA, LV, AA (right) during a representative heartbeat. Valves open and close, instantaneously, at the initial and final times of isovolumetric phases. We report these times also in Table 2.

mechanics is neglected. Furthermore, since we are modeling the cardiac valves with the RIIS method, weakly imposing a kinematic condition only, the dynamic balance is not fulfilled even between blood and valves. Thus, our computational model cannot correctly capture the physiological pressure transient during this phase, instead producing nonphysical and large oscillations. In Figure 13, we report the pressure transients in time and, for visualization purposes, we ignore the isovolumetric phases from the plot (grey boxes).

The ejection phase (Figure 15c and Figure 15d) is characterized by the opening of semilunar valves, the contraction of ventricles, and the blood flowing from the LV to the AO and from the RV to the PT. We measured peak flow rates equal to 398.74 mL/s and 478.16 mL/s, in the AV and PV, respectively, consistently with physiological values [130]. Moreover, as shown in Table 5, we found that also maximum velocities between AV and PV and peak ventricular pressures during ejection are always in physiological ranges.

During the isovolumetric relaxation, both the atrioventricular and semilunar valves are closed. The velocities measured are low compared to those of the other phases of the heartbeat. Furthermore, as for the isovolumetric contraction, the computational model cannot reproduce the typical pressure decrease occurring in this phase. On the contrary, large pressure oscillations arise.

During the ventricular passive filling, the blood flows from the pulmonary veins and the venae cavae into the LA and RA, respectively. Moreover, the atrioventricular valves are open and high-speed jets form between their leaflets. This moment corresponds to the E-wave of diastole (see Figure 14). Consistently with clinical measurements, the computational model is able to correctly reproduce the formation of the clockwise jet in the LV, redirecting the blood towards the outflow tract [134, 135]. Furthermore, from Table 5, we can observe that maximum velocity between MV and TV leaflets are in the physiological ranges. Furthermore, we also report average atrial pressure values and we found a general good agreement with reference data, even if left atrial pressure is slightly larger than our reference. To better appreciate how *in silico* results are in line with physiological ranges, we display each biomarker in Figure 12. As for Figure 9, we normalize each biomarker in the interval $[-1, 1]$ with respect to the physiological values listed in Table 5.

| Biomarker | | In silico | Physiological values | |
|------------------|--------|-----------|----------------------|-------|
| Peak MV velocity | [m/s] | 1.03 | 0.89 ± 0.15 | [133] |
| Peak AV velocity | [m/s] | 1.21 | 1.07 ± 0.18 | [136] |
| Peak TV velocity | [m/s] | 0.45 | 0.48 ± 0.11 | [137] |
| Peak PV velocity | [m/s] | 1.15 | 0.80 to 1.20 | [138] |
| Mean LA pressure | [mmHg] | 13.3 | 2 to 12 | [139] |
| Peak LV pressure | [mmHg] | 111 | 119 ± 13 | [131] |
| Mean RA pressure | [mmHg] | 6.33 | 0 to 8 | [139] |
| Peak RV pressure | [mmHg] | 37.0 | 35 ± 11 | [132] |

Table 5: Fluid dynamics biomarkers obtained with the whole-heart CFD simulation (normal ranges or mean \pm standard deviation). In silico values are computed by averaging fluid properties in spherical control volumes located between the valve leaflets (velocities) and in the heart chambers (pressures).

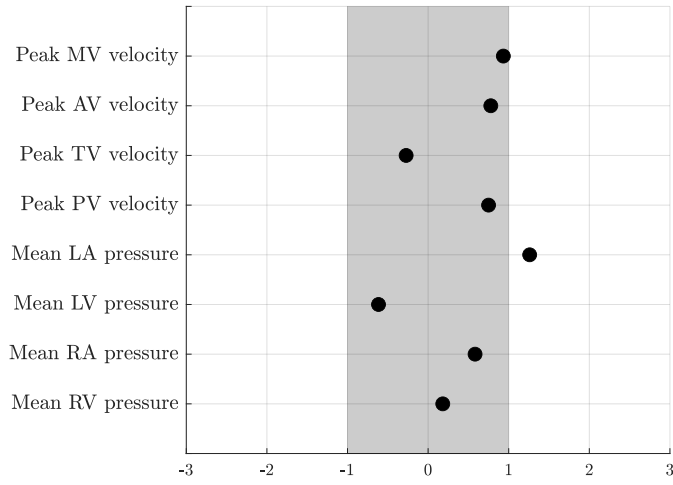


Figure 12: Fluid dynamics biomarkers obtained with the whole heart CFD simulations and normalized in the range $[-1, 1]$ with respect to the physiological ranges given in Table 5. The grey rectangle denotes the reference range.

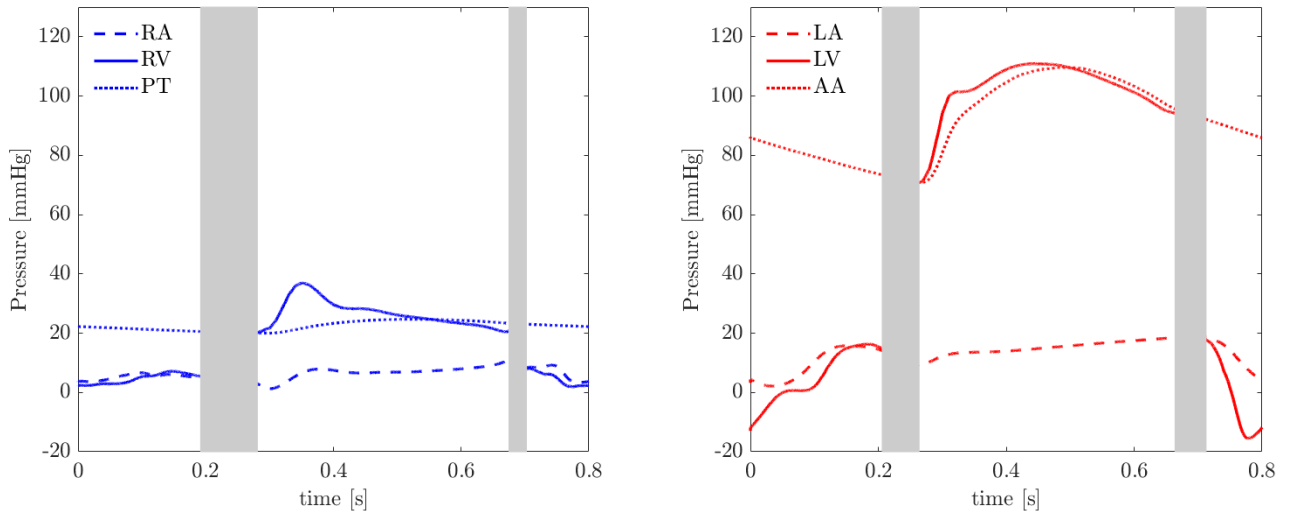


Figure 13: Pressure computed in control volumes located in RA, RV, PT (left) and LA, LV, AO (right) during a representative heartbeat. Isovolumetric phases are not considered, since the intraventricular pressure is not well defined when both valves are closed.

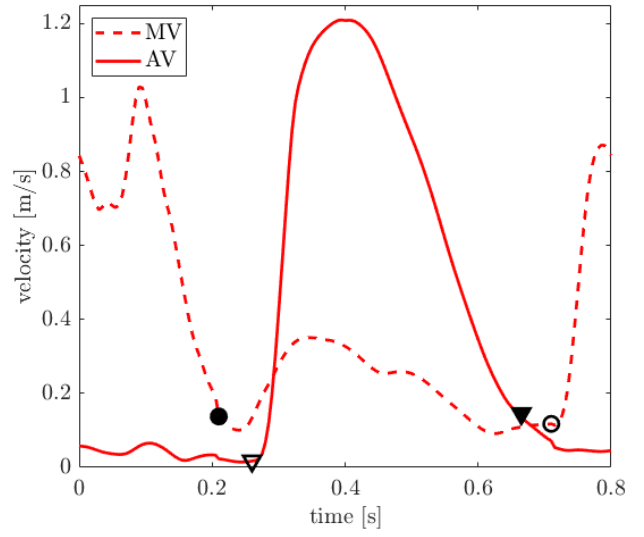
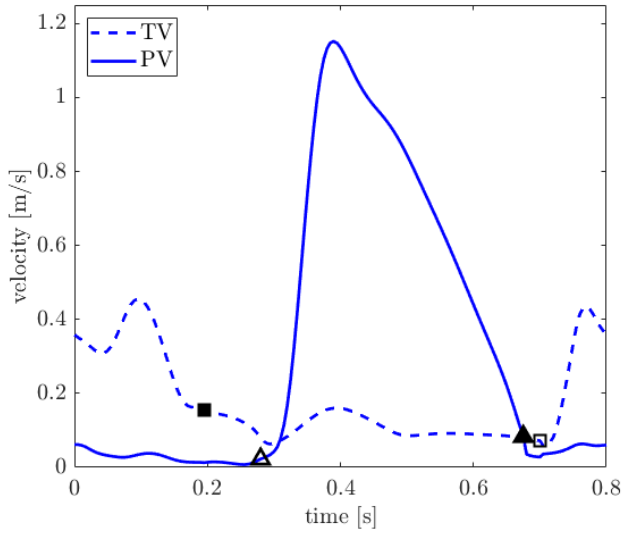


Figure 14: Velocity magnitudes computed in control volumes located between the valve leaflets: TV, PV (left) and MV, AV (right).

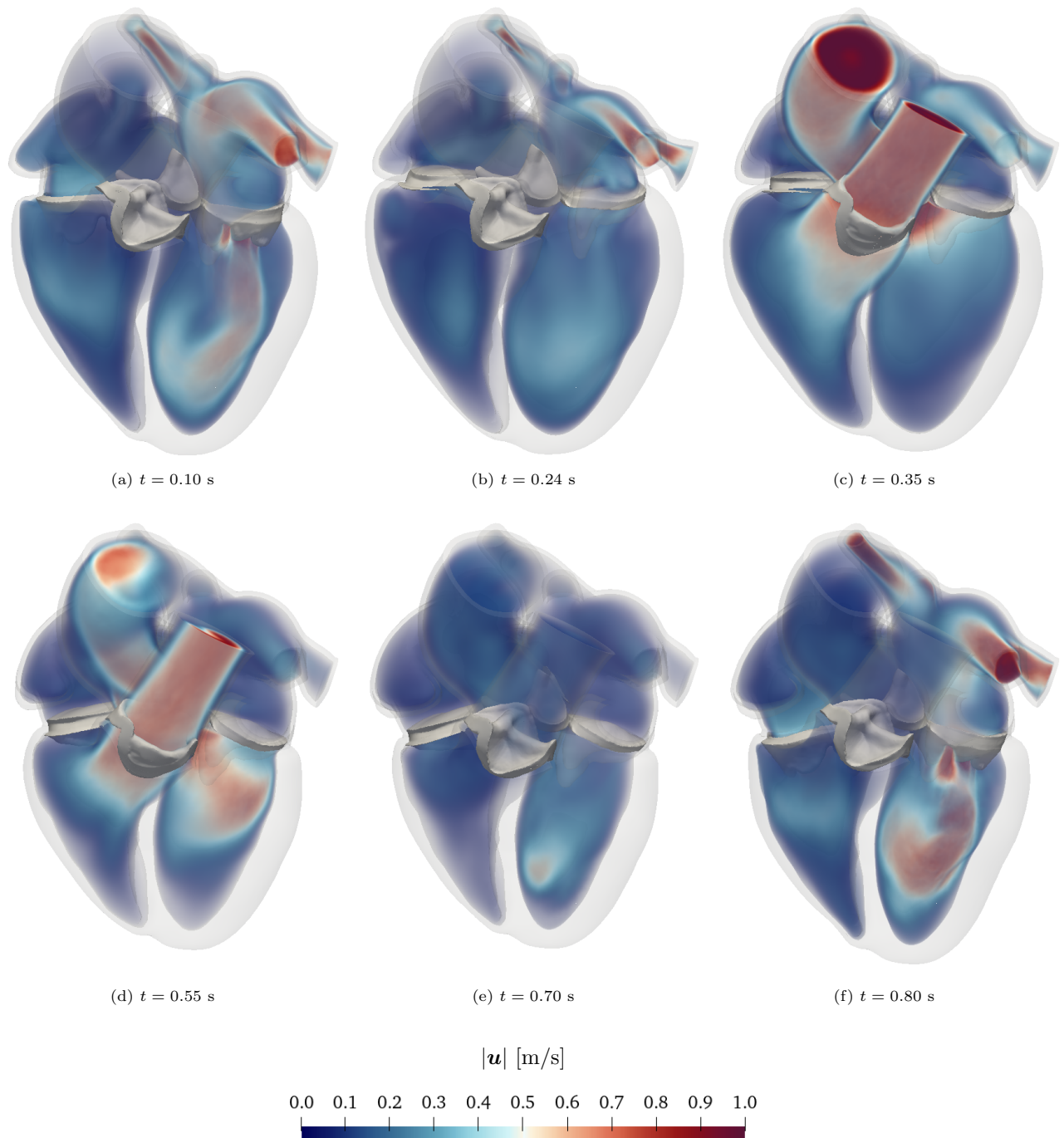
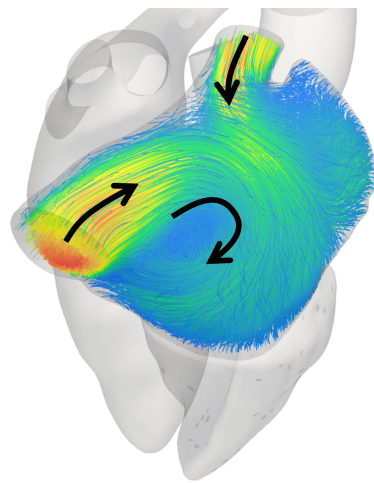
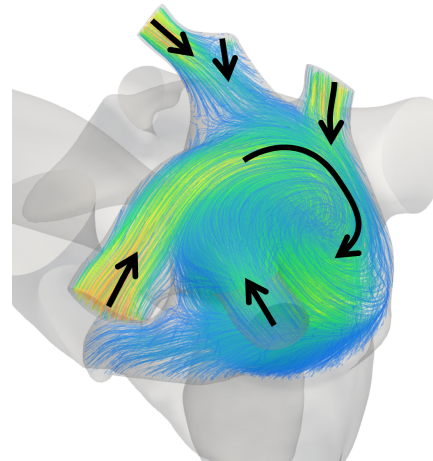


Figure 15: Volume rendering of velocity magnitude in different frames during the cardiac cycle: (a) diastolic a-wave peak, (b) isovolumetric contraction, (c) systolic peak, (d) mid systolic deceleration, (e) isovolumetric relaxation, (f) diastolic a-wave peak.

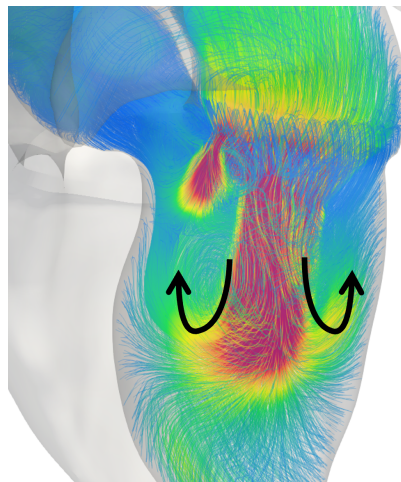
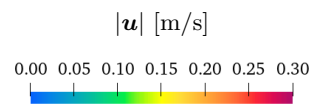
To better investigate blood flow patterns in the whole heart, we report the streamlines colored according to velocity magnitude in different chambers in Figure 16. We compare our *in silico* results with the MRI phase-velocity mapping visualization provided in Figure 1 of reference [135], and we found a good accordance. Specifically, Figure 16a shows the rotation of the blood in the RA as the chamber expands and the blood flows from the inferior and superior vena cava. Similarly, on the left side, the blood flows from the pulmonary veins to the expanding LA producing collision of blood jets and redirecting the flow towards the closed MV (see Figure 16b). During E-wave, as we show in Figure 16c, asymmetric recirculation is observed: shear layers roll through MV leaflets producing an O-vortex, as also seen in [1]. The counter-clockwise vortex under the posterior leaflet quickly disappears, and the clockwise vortex becomes larger and larger producing a clockwise jet, as described in [134], and clearly observed in Figure 16d.



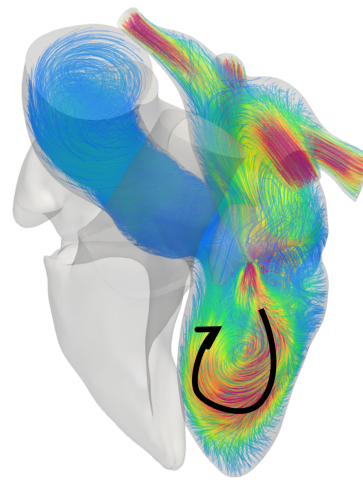
(a) Right atrium $t = 0.6$ s



(b) Left atrium $t = 0.6$ s



(c) Left ventricle $t = 0.775$ s



(d) Left heart $t = 0.8$ s

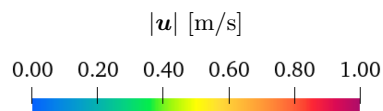


Figure 16: Streamlines colored according to velocity magnitude at different locations in the heart at different times: (a) right atrium during ventricular systole, (b) left atrium during ventricular systole, (c) clockwise and counter-clockwise vortices in the left ventricle during early diastole, (d) formation of clockwise jet in the left ventricle.

4.4. Application to a pathological scenario: Left Bundle Branch Block effects on hemodynamics

In this section, we apply our multiphysics computational model to investigate the hemodynamic consequences of the LBBB. This heart condition is commonly associated to an electrophysiological abnormality; however, it implies a cascade of adverse events due to the interaction among different physical processes. LBBB consists in a slow or even absent conduction through the left bundle branch, causing a dyssynchronous contraction and relaxation of the left ventricle. Moreover, the LV dyssynchrony may have profound consequences on the heart hemodynamics, influencing flow patterns and, in turn, triggering heart remodeling [140, 141].

To simulate LBBB with our EM model, we deactivate the impulse sites in the LV and in the septum (see Figure 17), so that the signal is generated by the SAN and the RVm sites solely. Our modeling choice is consistent with the work of [142], where a severe case of LBBB is accounted for by activating only one site in the RV free wall.

Figure 18 displays volumes and their derivatives with respect to time for left and right ventricles, in both physiological and LBBB conditions. The electrical dyssynchrony between left and right parts produces a delay in the LV ejection and filling stages. Differently, no significant differences are observed in the RV volumes. Furthermore, compared to the physiological case (see Table 4) and consistently with [140], we measured reduced ejection fractions both in the right (53.87%) and left (55.39%) ventricles. Furthermore, we observe a different motion of the intra-ventricular septum during the pre-ejection phase. As we display in Figure 19, the LBBB case is characterized by an abnormal leftward motion of the septum. Our result is consistent with different clinical observations [143, 144].

By means of our whole-heart EM driven CFD simulation, we can quantify how the pathology affects the endocardial wall stress. Let $\tau(\mathbf{u}) = 2\mu\epsilon(\mathbf{u})$ be the viscous stress tensor, we compute the wall shear stress vector as

$$\mathbf{WSS}(\mathbf{u}) = \tau(\mathbf{u})\mathbf{n} - (\tau(\mathbf{u})\mathbf{n} \cdot \mathbf{n})\mathbf{n} \quad \text{on } \partial\Omega_0 \times (0, T).$$

The time averaged wall shear stress (TAWSS) is then defined as

$$\text{TAWSS}(\mathbf{u}) = \frac{1}{T} \int_0^T |\mathbf{WSS}(\mathbf{u})| dt \quad \text{on } \partial\Omega_0.$$

Figure 20 shows the TAWSS in the right and left heart in physiological conditions and under LBBB. We notice that the TAWSS distribution is almost unchanged for the right heart. Conversely, we find that LBBB alters the wall shear stress in correspondence of the LV septum, suggesting the potential occurrence of remodeling phenomena. In Figure 21, we report the minimum, maximum and average WSS in the LV septum against time, for the physiological and LBBB simulations. During the ejection, the WSS values are similar, while significant differences are present during the filling phase. As a matter of fact, under LBBB, the space-averaged WSS peak is 27.4% higher than the physiological case (see Figure 21, right). This is consistent with the work of Eriksson *et al.* (2017), where they observed, by means of 4Dflow MRI data, that LV dyssynchronous motion influences blood flow patterns during diastole, contributing to the development of cardiac remodeling [141].

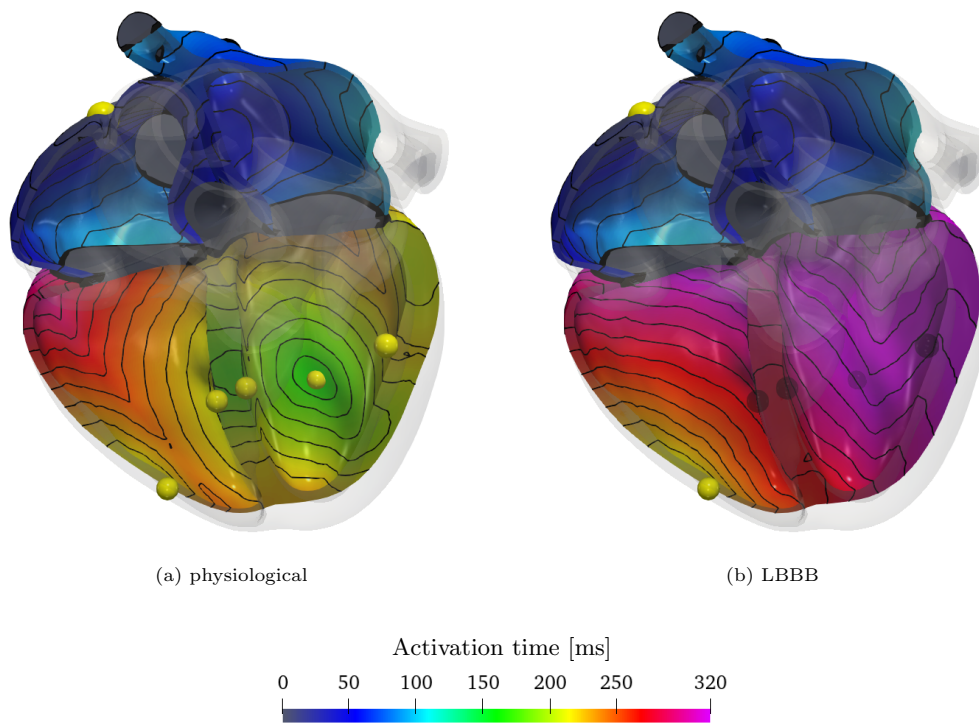


Figure 17: Activation maps and impulse sites (yellow spheres) in EM simulations; (a) physiological; (b) LBBB.

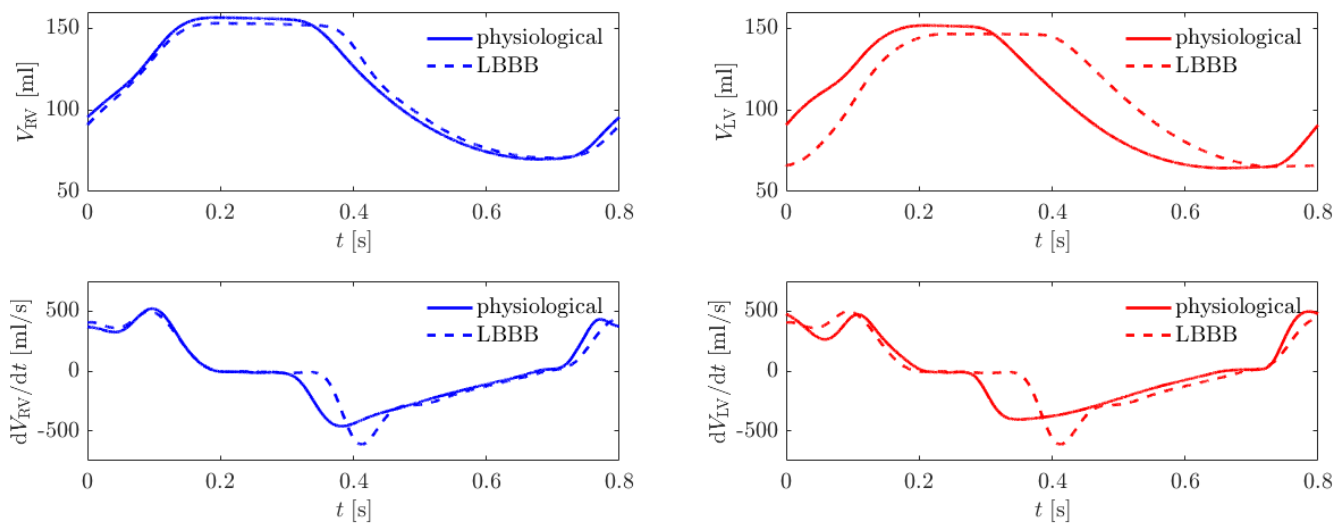


Figure 18: Ventricular volumes and ventricular volume derivatives for physiological and LBBB simulations.

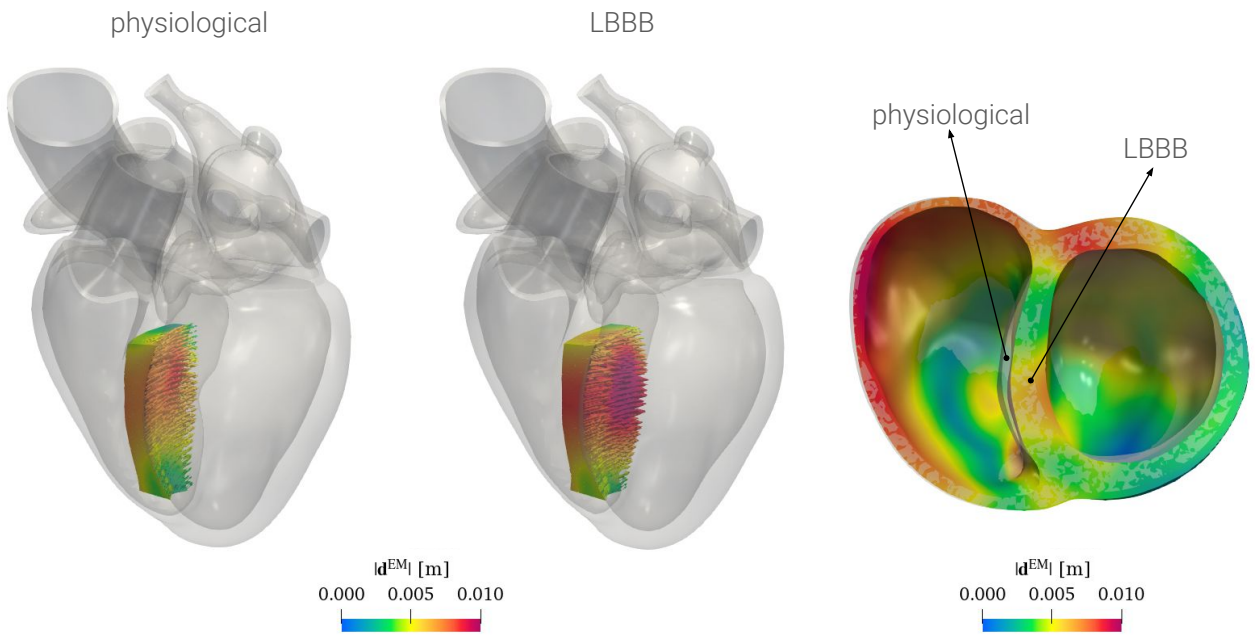


Figure 19: Comparison of the displacement field in the physiological and LBBB case at time $t = 0.31$ s. From the left to the right: septum colored according to displacement magnitude with glyphs of displacement in the physiological and LBBB case; top-view of the left and right ventricles (in transparent the physiological case, colored according to displacement magnitude the LBBB case).

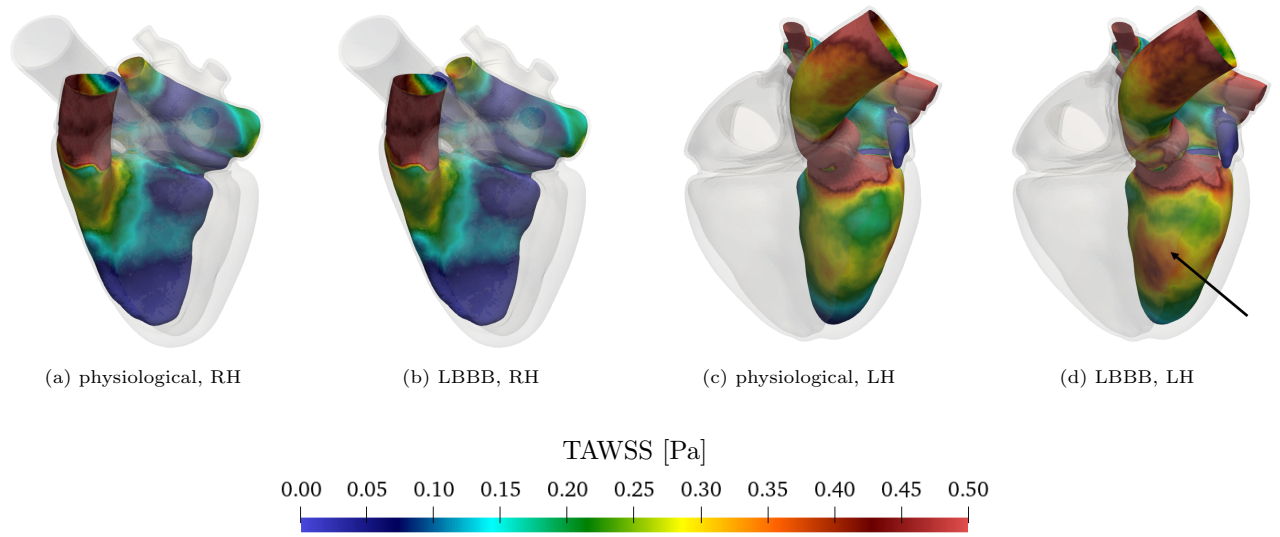


Figure 20: TAWSS of the whole heart in physiological and pathological conditions for the LH and RH. Results obtained with whole-heart EM-driven CFD simulations, the left and right parts are separated for visualization purposes. The largest differences are observed in the LV septum, as highlighted by the black arrow.

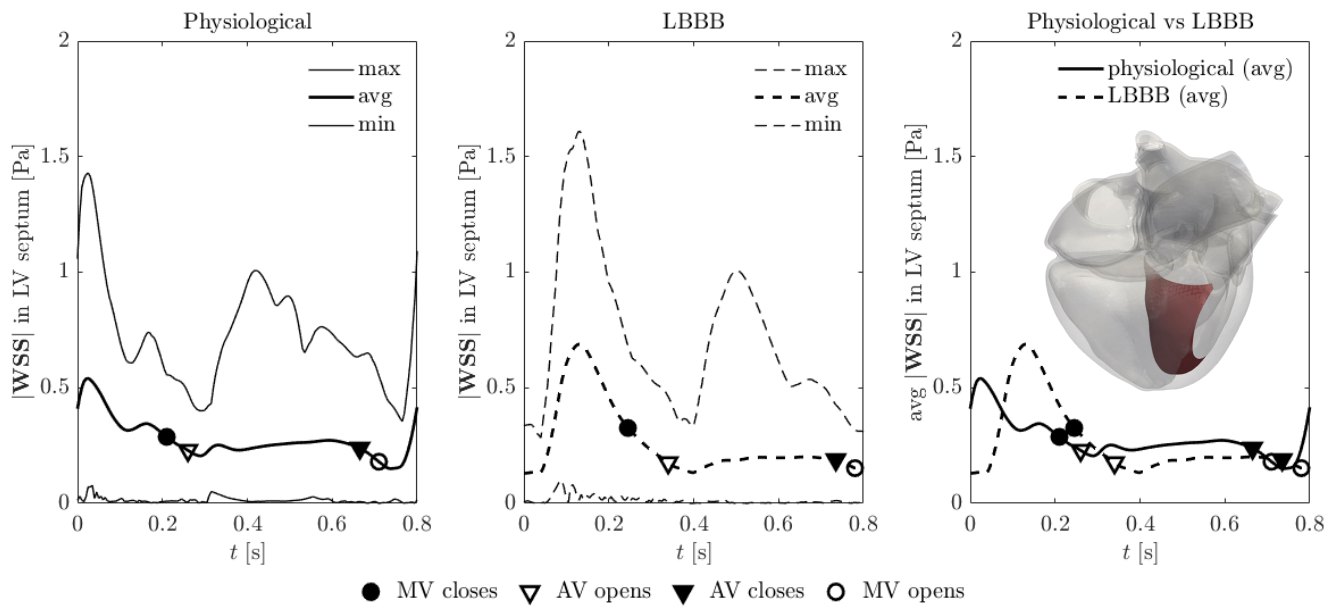


Figure 21: WSS in the LV septum over time. Maximum, average and minimum in physiological conditions (left); maximum, average and minimum in LBBB conditions (center); comparison between physiological and pathological conditions in terms of average values (right). The WSS is computed in the red portion shown on the right. In terms of maximum values, the pathological peak is 12.7% larger than the physiological case (cf. left and center figures). The average WSS peak increases of 27.4% (right figure).

5. Discussion, limitations, and further developments

We discuss some limitations of our study. The computational model introduced cannot fully represent the isovolumetric phases in terms of pressure. Indeed, when both valves are closed and the ventricles are contracting/relaxing at constant volumes, the pressure is not well-defined, and thus prone to spurious oscillations. This is due to the fact that we are using kinematic conditions only in all the ventricular boundaries. Indeed, we prescribe the EM displacement on the endocardium and endothelium, and we model valves with the RIIS method using a penalty-based kinematic condition. The oscillatory pressure during such phases does not influence the velocity field. However, it prevents from using the simulated pressure values to choose when to open and close the valves, forcing hence to prescribe a-priori opening and closing times. The use of bidirectionally coupled FSI models for the blood-myocardium or blood-valve systems (or for both of them) may allow to correctly capture the pressure transient during these phases, as seen for instance in [48] where a fully-coupled electro-mechano-fluid of the heart is considered.

Moreover, we noticed that the ejection phase is too slow and the ventricular passive filling too fast, if compared with medical literature values. Consequently, E-wave and A-wave are characterized by comparable amplitudes, whereas the EA ratio should be approximately equal to 1.30 ± 0.570 [133]. In this respect, we believe that the use of ionic models with a more realistic decrease of calcium concentration is essential to better capture these phenomena.

~~Finally, we applied the computational model to a realistic, templated heart geometry. In order to move towards the realization of whole heart digital twins, further developments should involve patient-specific cardiac simulations, accompanied with a stringent process of data assimilation, model validation and uncertainty quantification.~~

A small time step is needed in the CFD simulation, particularly during the fast dynamics of the ejection phase. An adaptive time-stepping scheme would mitigate the computational burden of the overall multiphysics computational model. This scheme would involve using a small time step during ejection and larger values during the remaining phases of the cardiac cycle.

Constructing a surrogate model would be a promising tool for expeditious calibration and sensitivity analysis. This model, incorporating inputs from both the EM and CFD models, along with outputs representing electrical, mechanical, and hemodynamical quantities of interest, would offer a mean to efficiently handle the complexity of the complex full order model. Previous works in the literature have successfully built such models for standalone cardiac electromechanics [145, 146, 147, 148] and standalone image-based hemodynamics [40].

Ensuring the “credibility evidence” for medical device submission of this intricate model would involve thorough verification and validation processes [149, 150]. For simplified models, such as cardiac electrophysiology and hemodynamics, we presented verification studies in our recent releases of `lifex` [116, 115], our FE cardiac solver. Differently, for this multiphysics model, drawing inspiration from practices in cardiac electrophysiology [151], the creation of a simplified benchmark (e.g., an idealized left ventricle) incorporating the coupling of electrophysiology, mechanics, and hemodynamics would facilitate systematic verification of model’s implementation.

Finally, moving towards model validation and the development of whole-heart digital twins, future efforts should focus on patient-specific cardiac simulations. Integrating various in vivo data sources, such as electrocardiograms, cine cardiac magnetic resonance, and 4D flow MRI data, for comparison with in silico results presents a substantial challenge. However, overcoming obstacles in data assimilation, model parametrization, and validation would become imperative, given the inherent uncertainties associated with such in vivo data.

6. Conclusions

In this paper, we introduced a computational model for the hemodynamics simulation of the whole human heart accounting for the main features affecting the intracardiac flows. We considered a realistic whole-heart geometry, and we employed a four-chamber 3D-0D electromechanical model to provide the displacement as input to the cardiac CFD model. We modelled the effect of cardiac valves in the fluid via a resistive immersed method and we accounted for transition-to-turbulence regime through the VMS-LES method. Moreover, for the first time, we coupled the 3D CFD model of the whole heart to the surrounding closed-loop circulation, to get a geometric multiscale 3D-0D hemodynamic model of the entire cardiovascular system. We solved our multiphysics and multiscale computational model using our in-house finite element library `lifex`.

We introduced a calibration of the active contraction model, driving the electromechanical simulation, aimed at obtaining physiological realistic flowrates, and consequently blood velocities, in the CFD simulation. Our calibration highlights the effect of the parameters of the active force generation model, associated to the microscopic features of its kinematics and of the force-velocity relationship, on the macroscopic heartbeat indicators.

We carried out EM-driven CFD simulation on a realistic whole-heart geometry and we showed that the computational model can correctly reproduce blood velocities and pressure traces when we compare the results with clinical ranges from medical literature. Furthermore, we found that the computational model captures typical blood flow patterns observed in MRI phase-velocity mapping visualizations.

Finally, we applied the whole-heart model to simulate the pathological scenario of Left Bundle Branch Block: we correctly predicted the electrical delay, the consequent mechanical dyssynchrony, a reduced ejection fraction, and an increasing wall shear stress in the left ventricular septum during the filling stage. Overall, this study confirms that the interaction of different physics in a high-fidelity integrated whole-heart model is essential for simulating the cardiac function, allowing to faithfully capture pathological events occurring at different physical levels.

Appendix A. The open 0D circulation model

The closed-loop lumped-parameter (0D) circulation model that we employ was proposed in [65] and inspired by [57, 152]. To couple the 0D model to the 3D model of the heart, we follow the same steps presented in [27]. Specifically, the open 0D system we get reads as follows: for any $t \in (0, T)$,

$$\frac{dp_{\text{AR}}^{\text{SYS}}(t)}{dt} = \frac{1}{C_{\text{AR}}^{\text{SYS}}} (Q_{\text{AV}}(t) - Q_{\text{AR}}^{\text{SYS}}(t)), \quad (\text{A.1a})$$

$$\frac{dp_{\text{VEN}}^{\text{SYS}}(t)}{dt} = \frac{1}{C_{\text{VEN}}^{\text{SYS}}} (Q_{\text{AR}}^{\text{SYS}}(t) - Q_{\text{VEN}}^{\text{SYS}}(t)), \quad (\text{A.1b})$$

$$\frac{dp_{\text{AR}}^{\text{PUL}}(t)}{dt} = \frac{1}{C_{\text{AR}}^{\text{PUL}}} (Q_{\text{PV}}(t) - Q_{\text{AR}}^{\text{PUL}}(t)), \quad (\text{A.1c})$$

$$\frac{dp_{\text{VEN}}^{\text{PUL}}(t)}{dt} = \frac{1}{C_{\text{VEN}}^{\text{PUL}}} (Q_{\text{AR}}^{\text{PUL}}(t) - Q_{\text{PUL}}^{\text{VEN}, 3\text{D}}(t)), \quad (\text{A.1d})$$

$$\frac{dQ_{\text{AR}}^{\text{SYS}}(t)}{dt} = \frac{R_{\text{AR}}^{\text{SYS}}}{L_{\text{AR}}^{\text{SYS}}} \left(-Q_{\text{AR}}^{\text{SYS}}(t) - \frac{p_{\text{VEN}}^{\text{SYS}}(t) - p_{\text{AR}}^{\text{SYS}}(t)}{R_{\text{AR}}^{\text{SYS}}} \right), \quad (\text{A.1e})$$

$$\frac{dQ_{\text{AR}}^{\text{PUL}}(t)}{dt} = \frac{R_{\text{AR}}^{\text{PUL}}}{L_{\text{AR}}^{\text{PUL}}} \left(-Q_{\text{AR}}^{\text{PUL}}(t) - \frac{p_{\text{VEN}}^{\text{PUL}}(t) - p_{\text{AR}}^{\text{PUL}}(t)}{R_{\text{AR}}^{\text{PUL}}} \right), \quad (\text{A.1f})$$

solved with suitable initial conditions, and

$$p_{\text{LA}}^{\text{in}}(t) = p_{\text{VEN}}^{\text{PUL}}(t) - R_{\text{VEN}}^{\text{PUL}} Q_{\text{VEN}}^{\text{PUL}}(t) - L_{\text{VEN}}^{\text{PUL}} \frac{dQ_{\text{VEN}}^{\text{PUL}, 3\text{D}}(t)}{dt}, \quad (\text{A.2a})$$

$$p_{\text{RA}}^{\text{in}}(t) = p_{\text{VEN}}^{\text{SYS}}(t) - R_{\text{VEN}}^{\text{SYS}} Q_{\text{VEN}}^{\text{SYS}}(t) - L_{\text{VEN}}^{\text{SYS}} \frac{dQ_{\text{VEN}}^{\text{SYS}, 3\text{D}}(t)}{dt}. \quad (\text{A.2b})$$

Appendix B. Setup of EM and CFD simulations

We report in this section the values of the parameters used in the EM and CFD simulations.

Table B.6 reports the parameters for the circulation model used in the EM simulation. With respect to the model presented in [64], we introduce two additional resistance elements ($R_{\text{upstream}}^{\text{SYS}}$ and $R_{\text{upstream}}^{\text{PUL}}$) and two inductance elements (L^{AV} , L^{PV} , see Figure 1c). They have the purpose of making the 0D circulation model, which surrogates the fluid dynamics, as similar as possible to the 3D CFD problem. For the same reason, the minimum resistances of the non-ideal diodes representing the AV and PV are increased with respect to [64].

The calibration of the RDQ20 active contraction model is extensively discussed in Section 4.2, and the corresponding parameter values are reported in Table 3. As reference sarcomere length, we set $\text{SL}_0 = 2.2 \mu\text{m}$. For all other parameters in the EM model, we use the same values as those of the baseline simulation of [64].

Table B.7 reports the values of the initial circulation states for the CFD simulation. They are taken equal to the values reached at the beginning of the last heartbeat in the EM simulation. All resistance, capacitance and inductance parameters are the same as in the EM model (see Table B.6).

| | Parameter | Value | |
|--------------------|--|-------------------|-------------------------|
| Systemic arteries | R_{AR}^{SYS} | 0.48 | mmHg s/mL |
| | C_{AR}^{SYS} | 1.50 | mL/mmHg |
| | L_{AR}^{SYS} | 0.005 | mmHg s ² /mL |
| | $R_{upstream}^{SYS}$ | 0.048 | mmHg s/mL |
| | $p_{AR,0}^{SYS}$ | 83.9 | mmHg |
| | $Q_{AR,0}^{SYS}$ | 0.0 | mL/s |
| Systemic veins | R_{VEN}^{SYS} | 0.26 | mmHg s/mL |
| | C_{VEN}^{SYS} | 60 | mL/mmHg |
| | L_{VEN}^{SYS} | $5 \cdot 10^{-4}$ | mmHg s ² /mL |
| | $p_{VEN,0}^{SYS}$ | 35.5 | mmHg |
| | $Q_{VEN,0}^{SYS}$ | 0.0 | mL/s |
| Pulmonary arteries | R_{AR}^{PUL} | 0.032116 | mmHg s/mL |
| | C_{AR}^{PUL} | 10 | mL/mmHg |
| | L_{AR}^{PUL} | 0.0005 | mmHg s ² /mL |
| | $R_{upstream}^{PUL}$ | 0.0032116 | mmHg s/mL |
| | $p_{AR,0}^{PUL}$ | 14.90 | mmHg |
| | $Q_{AR,0}^{PUL}$ | 0.0 | mL/s |
| Pulmonary veins | R_{VEN}^{PUL} | 0.035684 | mmHg s/mL |
| | C_{VEN}^{PUL} | 16 | mL/mmHg |
| | L_{VEN}^{PUL} | 0.0005 | mmHg s ² /mL |
| | $p_{VEN,0}^{PUL}$ | 13.58 | mmHg |
| | $Q_{VEN,0}^{PUL}$ | 0.0 | mL/s |
| Valves | R_{min}^{MV} | 0.0075 | mmHg s/mL |
| | R_{min}^{AV} | 0.0355 | mmHg s/mL |
| | R_{min}^{TV} | 0.0075 | mmHg s/mL |
| | R_{min}^{PV} | 0.0184 | mmHg s/mL |
| | $R_{max}^{MV}, R_{max}^{AV}, R_{max}^{TV}, R_{max}^{PV}$ | 75006.2 | mmHg s/mL |
| | L^{AV}, L^{PV} | $5 \cdot 10^{-4}$ | mmHg s ² /mL |

Table B.6: Parameters and initial conditions of the circulation model used for the EM simulation.

| | Parameter | Value | |
|--------------------|-------------------|----------|------|
| Systemic arteries | $p_{AR,0}^{SYS}$ | 86.3480 | mmHg |
| | $Q_{AR,0}^{SYS}$ | 109.6429 | mL/s |
| Systemic veins | $p_{VEN,0}^{SYS}$ | 34.4923 | mmHg |
| | $Q_{VEN,0}^{SYS}$ | 112.9209 | mL/s |
| Pulmonary arteries | $p_{AR,0}^{PUL}$ | 22.2310 | mmHg |
| | $Q_{AR,0}^{PUL}$ | 83.2132 | mL/s |
| Pulmonary veins | $p_{VEN,0}^{PUL}$ | 19.5813 | mmHg |
| | $Q_{VEN,0}^{PUL}$ | 262.6397 | mL/s |

Table B.7: Initial states of the circulation model for the CFD simulation. The values are equal to those of the circulation state variables at the beginning of the last heartbeat in the EM simulation. All remaining circulation parameters (resistances, capacitances, inductances) are the same as in the EM model (see Table B.6).

Acknowledgments

AZ, LD and AQ received funding from the Italian Ministry of University and Research (MIUR) within the PRIN (Research projects of relevant national interest) 2017 “Modeling the heart across the scales: from cardiac cells to the whole organ” Grant Registration number 2017AXL54F).

MB, RP, FR, LD and AQ acknowledge the ERC Advanced Grant iHEART, “An Integrated Heart Model for the simulation of the cardiac function”, 2017–2023, P.I. A. Quarteroni (ERC–2016– ADG, project ID: 740132).



The authors of this work are members of the INdAM group GNCS “Gruppo Nazionale per il Calcolo Scientifico” (National Group for Scientific Computing).

We acknowledge the CINECA award under the ISCRA initiative, for the availability of high performance computing resources and support under the projects IsC87_MCH, P.I. A. Zingaro, 2021-2022 and IsB25_MathBeat, P.I. A. Quarteroni, 2021-2022.

The present research is part of the activities of 650 “Dipartimento di Eccellenza 2023-2027”, MIUR, Italy

References

- [1] C. Chnafa, S. Mendez, F. Nicoud, Image-based large-eddy simulation in a realistic left heart, *Computers & Fluids* 94 (2014) 173–187.
- [2] A. This, L. Boilevin-Kayl, M. A. Fernández, J.-F. Gerbeau, Augmented resistive immersed surfaces valve model for the simulation of cardiac hemodynamics with isovolumetric phases, *International Journal for Numerical Methods in Biomedical Engineering* 36 (2020) e3223.
- [3] A. Tagliabue, L. Dede’, A. Quarteroni, Complex blood flow patterns in an idealized left ventricle: A numerical study, *Chaos: An Interdisciplinary Journal of Nonlinear Science* 27 (2017) 093939.
- [4] A. Tagliabue, L. Dede’, A. Quarteroni, Fluid dynamics of an idealized left ventricle: the extended nitsche’s method for the treatment of heart valves as mixed time varying boundary conditions, *International Journal for Numerical Methods in Fluids* 85 (2017) 135–164.
- [5] I. Fumagalli, M. Fedele, C. Vergara, L. Dede’, S. Ippolito, F. Nicolò, C. Antona, R. Scrofani, A. Quarteroni, An image-based computational hemodynamics study of the systolic anterior motion of the mitral valve, *Computers in Biology and Medicine* 123 (2020) 103922.
- [6] E. Karabelas, M. A. Gsell, C. M. Augustin, L. Marx, A. Neic, A. J. Prassl, L. Goubergrits, T. Kuehne, G. Plank, Towards a computational framework for modeling the impact of aortic coarctations upon left ventricular load, *Frontiers in Physiology* 9 (2018) 538.
- [7] A. This, H. G. Morales, O. Bonnefous, M. A. Fernández, J.-F. Gerbeau, A pipeline for image based intracardiac CFD modeling and application to the evaluation of the PISA method, *Computer Methods in Applied Mechanics and Engineering* 358 (2020) 112627.
- [8] A. Masci, M. Alessandrini, D. Forti, F. Menghini, L. Dede’, C. Tomasi, A. Quarteroni, C. Corsi, A proof of concept for computational fluid dynamic analysis of the left atrium in atrial fibrillation on a patient-specific basis, *Journal of Biomechanical Engineering* 142 (2020).
- [9] F. Viola, V. Meschini, R. Verzicco, Fluid–Structure–Electrophysiology interaction (FSEI) in the left-heart: a multi-way coupled computational model, *European Journal of Mechanics-B/Fluids* 79 (2020) 212–232.
- [10] J. O. Mangual, E. Kraigher-Krainer, A. De Luca, L. Toncelli, A. Shah, S. Solomon, G. Galanti, F. Domenichini, G. Pedrizzetti, Comparative numerical study on left ventricular fluid dynamics after dilated cardiomyopathy, *Journal of Biomechanics* 46 (2013) 1611–1617.

- [11] X. Zheng, J. Seo, V. Vedula, T. Abraham, R. Mittal, Computational modeling and analysis of intracardiac flows in simple models of the left ventricle, *European Journal of Mechanics-B/Fluids* 35 (2012) 31–39.
- [12] J. H. Seo, V. Vedula, T. Abraham, A. C. Lardo, F. Dawoud, H. Luo, R. Mittal, Effect of the mitral valve on diastolic flow patterns, *Physics of Fluids* 26 (2014) 121901.
- [13] J. H. Seo, R. Mittal, Effect of diastolic flow patterns on the function of the left ventricle, *Physics of Fluids* 25 (2013) 110801.
- [14] A. Masci, M. Alessandrini, D. Forti, F. Menghini, L. Dede', C. Tommasi, A. Quarteroni, C. Corsi, A patient-specific computational fluid dynamics model of the left atrium in atrial fibrillation: Development and initial evaluation, in: *International Conference on Functional Imaging and Modeling of the Heart*, Springer, 2017, pp. 392–400.
- [15] A. Masci, L. Barone, L. Dedè, M. Fedele, C. Tomasi, A. Quarteroni, C. Corsi, The impact of left atrium appendage morphology on stroke risk assessment in atrial fibrillation: a computational fluid dynamics study, *Frontiers in Physiology* 9 (2019) 1938.
- [16] A. Zingaro, L. Dede', F. Menghini, A. Quarteroni, Hemodynamics of the heart's left atrium based on a variational multiscale-les numerical method, *European Journal of Mechanics-B/Fluids* 89 (2021) 380–400.
- [17] M. Corti, L. Dede', A. Zingaro, A. Quarteroni, Impact of atrial fibrillation on left atrium haemodynamics: A computational fluid dynamics study, *Computers in Biology and Medicine* (2022) 106143.
- [18] V. Vedula, R. George, L. Younes, R. Mittal, Hemodynamics in the left atrium and its effect on ventricular flow patterns, *Journal of Biomechanical Engineering* 137 (2015).
- [19] R. Koizumi, K. Funamoto, T. Hayase, Y. Kanke, M. Shibata, Y. Shiraishi, T. Yambe, Numerical analysis of hemodynamic changes in the left atrium due to atrial fibrillation, *Journal of Biomechanics* 48 (2015) 472–478.
- [20] D. Dillon-Murphy, D. Marlevi, B. Ruijsink, A. Qureshi, H. Chubb, E. Kerfoot, M. O'Neill, D. Nordsletten, O. Aslanidi, A. De Vecchi, Modeling left atrial flow, energy, blood heating distribution in response to catheter ablation therapy, *Frontiers in Physiology* 9 (2018) 1757.
- [21] G. M. Bosi, A. Cook, R. Rai, L. J. Menezes, S. Schievano, R. Torii, G. Burriesci, Computational fluid dynamic analysis of the left atrial appendage to predict thrombosis risk, *Frontiers in Cardiovascular Medicine* 5 (2018) 34.
- [22] O. Mazumder, S. Gupta, D. Roy, A. Sinha, Computational fluid dynamic model of left atrium to analyze hemodynamic manifestation during atrial fibrillation, in: *2022 44th Annual International Conference of the IEEE Engineering in Medicine & Biology Society (EMBC)*, IEEE, 2022, pp. 3967–3971.
- [23] A. Zingaro, Z. Ahmad, E. Kholmovski, K. Sakata, L. Dede', A. K. Morris, A. Quarteroni, N. A. Trayanova, A comprehensive stroke risk assessment by combining atrial computational fluid dynamics simulations and functional patient data, *bioRxiv* (2024) 2024–01.
- [24] F. Viola, V. Meschini, R. Verzicco, An fsei approach for the assessment of stenotic aortic valve effects on the left heart hemodynamics, *Computers & Fluids* 265 (2023) 106017.
- [25] F. Viola, V. Spandan, V. Meschini, J. Romero, M. Fatica, M. D. de Tullio, R. Verzicco, FSEI-GPU: GPU accelerated simulations of the fluid–structure–electrophysiology interaction in the left heart, *Computer Physics Communications* 273 (2022) 108248.
- [26] L. Dede', F. Menghini, A. Quarteroni, Computational fluid dynamics of blood flow in an idealized left human heart, *International Journal for Numerical Methods in Biomedical Engineering* 37 (2021) e3287.
- [27] A. Zingaro, I. Fumagalli, L. Dede', M. Fedele, P. C. Africa, A. F. Corno, A. M. Quarteroni, A geometric multiscale model for the numerical simulation of blood flow in the human left heart, *Discrete and Continuous Dynamical System - S* 15 (2022) 2391–2427.
- [28] A. Zingaro, C. Vergara, L. Dede', F. Regazzoni, A. Quarteroni, A comprehensive mathematical model for cardiac perfusion, *Scientific Reports* 13 (2023) 14220.

- [29] L. Bennati, C. Vergara, V. Giambruno, I. Fumagalli, A. F. Corno, A. Quarteroni, G. Puppini, G. B. Luciani, An image-based computational fluid dynamics study of mitral regurgitation in presence of prolapse, *Cardiovascular Engineering and Technology* (2023) 1–19.
- [30] L. Bennati, V. Giambruno, F. Renzi, V. Di Nicola, C. Maffei, G. Puppini, G. B. Luciani, C. Vergara, Turbulent blood dynamics in the left heart in the presence of mitral regurgitation: a computational study based on multi-series cine-mri, *Biomechanics and Modeling in Mechanobiology* 22 (2023) 1829–1846.
- [31] L. Bennati, G. Puppini, V. Giambruno, G. Luciani, C. Vergara, Image-based computational fluid dynamics to compare two mitral valve reparative techniques for the prolapse, *bioRxiv* (2023) 2023–12.
- [32] F. Renzi, C. Vergara, M. Fedele, V. Giambruno, A. Quarteroni, G. Puppini, G. B. Luciani, Accurate and efficient 3d reconstruction of right heart shape and motion from multi-series cine-mri, *bioRxiv* (2023) 2023–06.
- [33] H. Wiputra, C. Q. Lai, G. L. Lim, J. J. W. Heng, L. Guo, S. M. Soomar, H. L. Leo, A. Biwas, C. N. Z. Mattar, C. H. Yap, Fluid mechanics of human fetal right ventricles from image-based computational fluid dynamics using 4d clinical ultrasound scans, *American Journal of Physiology-Heart and Circulatory Physiology* 311 (2016) H1498–H1508.
- [34] D. Colli, L. Zovatto, G. Tonti, G. Pedrizzetti, Comparative analysis of right ventricle fluid dynamics, *Frontiers in Bioengineering and Biotechnology* 9 (2021).
- [35] J. Mangual, F. Domenichini, G. Pedrizzetti, Describing the highly three dimensional right ventricle flow, *Annals of Biomedical Engineering* 40 (2012) 1790–1801.
- [36] V. Mihalef, R. I. Ionasec, P. Sharma, B. Georgescu, I. Voigt, M. Suehling, D. Comaniciu, Patient-specific modelling of whole heart anatomy, dynamics and haemodynamics from four-dimensional cardiac CT images, *Interface Focus* 1 (2011) 286–296.
- [37] J.-i. Okada, T. Washio, S. Sugiura, T. Hisada, Clinical and pharmacological application of multiscale multi-physics heart simulator, *UT-heart*, *The Korean Journal of Physiology & Pharmacology* 23 (2019) 295–303.
- [38] M. Peirlinck, F. S. Costabal, J. Yao, J. Guccione, S. Tripathy, Y. Wang, D. Ozturk, P. Segars, T. Morrison, S. Levine, E. Kuhl, Precision medicine in human heart modeling, *Biomechanics and modeling in mechanobiology* 20 (2021) 803–831.
- [39] J. Brenneisen, A. Daub, T. Gerach, E. Kovacheva, L. Huetter, B. Frohnapfel, O. Dössel, A. Loewe, Sequential coupling shows minor effects of fluid dynamics on myocardial deformation in a realistic whole-heart model, *Frontiers in Cardiovascular Medicine* (2021) 1967.
- [40] E. Karabelas, S. Longobardi, J. Fuchsberger, O. Razeghi, C. Rodero, M. Strocchi, R. Rajani, G. Haase, G. Plank, S. Niederer, Global sensitivity analysis of four chamber heart hemodynamics using surrogate models, *IEEE Transactions on Biomedical Engineering* (2022).
- [41] F. Viola, G. Del Corso, R. De Paulis, R. Verzicco, GPU accelerated digital twins of the human heart open new routes for cardiovascular research, *Research Square* (2022).
- [42] J. Fuchsberger, P. Aigner, S. Niederer, G. Plank, H. Schima, G. Haase, E. Karabelas, On the incorporation of obstacles in a fluid flow problem using a navier–stokes–brinkman penalization approach, *Journal of Computational Science* 57 (2022) 101506.
- [43] A. Quarteroni, L. Dede, A. Manzoni, C. Vergara, *Mathematical Modelling of the Human Cardiovascular System: Data, Numerical Approximation, Clinical Applications*, volume 33, Cambridge University Press, 2019.
- [44] Y. J. Choi, J. Constantino, V. Vedula, N. Trayanova, R. Mittal, A new mri-based model of heart function with coupled hemodynamics and application to normal and diseased canine left ventricles, *Frontiers in bioengineering and biotechnology* 3 (2015) 140.
- [45] A. Santiago, J. Aguado-Sierra, M. Zavala-Aké, R. Doste-Beltran, S. Gómez, R. Arís, J. C. Cajas, E. Casoni, M. Vázquez, Fully coupled fluid-electro-mechanical model of the human heart for supercomputers, *International Journal for Numerical Methods in Biomedical Engineering* 34 (2018) e3140.

- [46] A. Santiago, Fluid-electro-mechanical model of the human heart for supercomputers, Ph.D. thesis, Universitat Politècnica de Catalunya, 2018. URL: <https://upcommons.upc.edu/bitstream/handle/2117/116302/TAS1de1+mod..pdf?sequence=5>.
- [47] A. Gerbi, Numerical approximation of cardiac electro-fluid-mechanical models: Coupling strategies for large-scale simulation, Ph.D. thesis, Ecole Polytechnique Fédérale de Lausanne, 2018.
- [48] M. Bucelli, A. Zingaro, P. C. Africa, I. Fumagalli, L. Dede', A. M. Quarteroni, A mathematical model that integrates cardiac electrophysiology, mechanics and fluid dynamics: application to the human left heart, *International Journal for Numerical Methods in Biomedical Engineering* (2022) e3678.
- [49] F. Domenichini, G. Pedrizzetti, B. Baccani, Three-dimensional filling flow into a model left ventricle, *Journal of fluid mechanics* 539 (2005) 179–198.
- [50] B. Baccani, F. Domenichini, G. Pedrizzetti, Vortex dynamics in a model left ventricle during filling, *European Journal of Mechanics-B/Fluids* 21 (2002) 527–543.
- [51] A. Santiago, C. Butakoff, B. Eguzkitza, R. A. Gray, K. May-Newman, P. Pathmanathan, V. Vu, M. Vázquez, Design and execution of a verification, validation, and uncertainty quantification plan for a numerical model of left ventricular flow after lvad implantation, *PLoS computational biology* 18 (2022) e1010141.
- [52] C. M. Augustin, A. Crozier, A. Neic, A. J. Prassl, E. Karabelas, T. Ferreira da Silva, J. F. Fernandes, F. Campos, T. Kuehne, G. Plank, Patient-specific modeling of left ventricular electromechanics as a driver for haemodynamic analysis, *EP Europace* 18 (2016) iv121–iv129.
- [53] A. Zingaro, M. Bucelli, I. Fumagalli, L. Dede', A. Quarteroni, Modeling isovolumetric phases in cardiac flows by an augmented resistive immersed implicit surface method, *International Journal for Numerical Methods in Biomedical Engineering* 39 (2023) e3767.
- [54] A. Zingaro, Mathematical and numerical models for the fluid dynamics of the human heart, Ph.D. thesis, Politecnico di Milano, 2022. URL: <https://hdl.handle.net/10589/189932>.
- [55] A. This, Image/model fusion for the quantification of mitral regurgitation severity, Ph.D. thesis, Sorbonne université, 2019.
- [56] A. Quarteroni, A. Veneziani, C. Vergara, Geometric multiscale modeling of the cardiovascular system, between theory and practice, *Computer Methods in Applied Mechanics and Engineering* 302 (2016) 193–252.
- [57] P. J. Blanco, R. A. Feijóo, A 3d-1d-0d computational model for the entire cardiovascular system, *Mecánica Computacional* 29 (2010) 5887–5911.
- [58] Y. Shi, T. Korakianitis, Numerical simulation of cardiovascular dynamics with left heart failure and in-series pulsatile ventricular assist device, *Artificial Organs* 30 (2006) 929–948.
- [59] V. Milišić, A. Quarteroni, Analysis of lumped parameter models for blood flow simulations and their relation with 1d models, *ESAIM: Mathematical modelling and numerical analysis* 38 (2004) 613–632.
- [60] H. J. Kim, I. E. Vignon-Clementel, C. A. Figueroa, J. F. LaDisa, K. E. Jansen, J. A. Feinstein, C. A. Taylor, On coupling a lumped parameter heart model and a three-dimensional finite element aorta model, *Annals of biomedical engineering* 37 (2009) 2153–2169.
- [61] F. N. Van de Vosse, N. Stergiopoulos, Pulse wave propagation in the arterial tree, *Annual Review of Fluid Mechanics* 43 (2011) 467–499.
- [62] L. Formaggia, D. Lamponi, A. Quarteroni, One-dimensional models for blood flow in arteries, *Journal of engineering mathematics* 47 (2003) 251–276.
- [63] L. Formaggia, J.-F. Gerbeau, F. Nobile, A. Quarteroni, On the coupling of 3d and 1d navier–stokes equations for flow problems in compliant vessels, *Computer Methods in Applied Mechanics and Engineering* 191 (2001) 561–582.
- [64] M. Fedele, R. Piersanti, F. Regazzoni, M. Salvador, P. C. Africa, M. Bucelli, A. Zingaro, A. Quarteroni, et al., A comprehensive and biophysically detailed computational model of the whole human heart electromechanics, *Computer Methods in Applied Mechanics and Engineering* 410 (2023) 115983.

- [65] F. Regazzoni, M. Salvador, P. Africa, M. Fedele, L. Dedè, A. Quarteroni, A cardiac electromechanical model coupled with a lumped-parameter model for closed-loop blood circulation, *Journal of Computational Physics* 457 (2022) 111083.
- [66] C. M. Augustin, M. A. Gsell, E. Karabelas, E. Willemen, F. W. Prinzen, J. Lumens, E. J. Vigmond, G. Plank, A computationally efficient physiologically comprehensive 3d-0d closed-loop model of the heart and circulation, *Computer Methods in Applied Mechanics and Engineering* 386 (2021) 114092.
- [67] F. Marcinno', A. Zingaro, I. Fumagalli, L. Dede, C. Vergara, A computational study of blood flow dynamics in the pulmonary arteries, *Vietnam Journal of Mathematics* (2022) 1–23.
- [68] X. Ma, H. Gao, B. E. Griffith, C. Berry, X. Luo, Image-based fluid–structure interaction model of the human mitral valve, *Computers & Fluids* 71 (2013) 417–425.
- [69] K. Kunzelman, D. R. Einstein, R. Cochran, Fluid–structure interaction models of the mitral valve: function in normal and pathological states, *Philosophical Transactions of the Royal Society B: Biological Sciences* 362 (2007) 1393–1406.
- [70] B. Su, L. Zhong, X.-K. Wang, J.-M. Zhang, R. San Tan, J. C. Allen, S. K. Tan, S. Kim, H. L. Leo, Numerical simulation of patient-specific left ventricular model with both mitral and aortic valves by FSI approach, *Computer methods and programs in biomedicine* 113 (2014) 474–482.
- [71] H. Gao, L. Feng, N. Qi, C. Berry, B. E. Griffith, X. Luo, A coupled mitral valve—left ventricle model with fluid–structure interaction, *Medical Engineering & Physics* 47 (2017) 128–136.
- [72] J. De Hart, G. Peters, P. Schreurs, F. Baaijens, A three-dimensional computational analysis of fluid–structure interaction in the aortic valve, *Journal of Biomechanics* 36 (2003) 103–112.
- [73] C. Carmody, G. Burriesci, I. Howard, E. Patterson, An approach to the simulation of fluid–structure interaction in the aortic valve, *Journal of Biomechanics* 39 (2006) 158–169.
- [74] D. Oks, M. Vázquez, G. Houzeaux, C. Butakoff, C. Samaniego, Fluid-structure interaction analysis of eccentricity and leaflet rigidity on thrombosis biomarkers in bioprosthetic aortic valve replacements, *International Journal for Numerical Methods in Biomedical Engineering* (2022) e3649.
- [75] J. Hiromi Spühler, J. Hoffman, An interface-tracking unified continuum model for fluid-structure interaction with topology change and full-friction contact with application to aortic valves, *International Journal for Numerical Methods in Engineering* 122 (2021) 5258–5278.
- [76] J. H. Spühler, J. Jansson, N. Jansson, J. Hoffman, 3d fluid-structure interaction simulation of aortic valves using a unified continuum ale fem model, *Frontiers in Physiology* 9 (2018) 363.
- [77] M. Fedele, E. Faggiano, L. Dede', A. Quarteroni, A patient-specific aortic valve model based on moving resistive immersed implicit surfaces, *Biomechanics and Modeling in Mechanobiology* 16 (2017) 1779–1803.
- [78] M. A. Fernández, J.-F. Gerbeau, V. Martin, Numerical simulation of blood flows through a porous interface, *ESAIM: Mathematical Modelling and Numerical Analysis* 42 (2008) 961–990.
- [79] M. Astorino, J. Hamers, S. C. Shadden, J.-F. Gerbeau, A robust and efficient valve model based on resistive immersed surfaces, *International Journal for Numerical Methods in Biomedical Engineering* 28 (2012) 937–959.
- [80] A. This, L. Boilevin-Kayl, M. A. Fernández, J.-F. Gerbeau, Augmented resistive immersed surfaces valve model for the simulation of cardiac hemodynamics with isovolumetric phases, *International Journal for Numerical Methods in Biomedical Engineering* 36 (2019).
- [81] F. Regazzoni, L. Dedè, A. Quarteroni, Biophysically detailed mathematical models of multiscale cardiac active mechanics, *PLOS Computational Biology* 16 (2020) e1008294.
- [82] N. Y. Tan, C. M. Witt, J. K. Oh, Y.-M. Cha, Left bundle branch block: current and future perspectives, *Circulation: Arrhythmia and Electrophysiology* 13 (2020) e008239.

- [83] R. Piersanti, F. Regazzoni, M. Salvador, A. F. Corno, L. Dede', C. Vergara, A. Quarteroni, 3D–0D closed-loop model for the simulation of cardiac biventricular electromechanics, *Computer Methods in Applied Mechanics and Engineering* 391 (2022) 114607.
- [84] R. Piersanti, *Mathematical and Numerical Modeling of Cardiac Fiber Generation and Electromechanical Function : Towards a Realistic Simulation of the Whole Heart*, Ph.D. thesis, Politecnico di Milano, 2022. URL: <http://hdl.handle.net/10589/183040>.
- [85] R. Piersanti, P. C. Africa, M. Fedele, C. Vergara, L. Dedè, A. F. Corno, A. Quarteroni, Modeling cardiac muscle fibers in ventricular and atrial electrophysiology simulations, *Computer Methods in Applied Mechanics and Engineering* 373 (2021) 113468.
- [86] R. Doste, D. Soto-Iglesias, G. Bernardino, A. Alcaine, R. Sebastian, S. Giffard-Roisin, M. Sermesant, A. Berruezo, D. Sanchez-Quintana, O. Camara, A rule-based method to model myocardial fiber orientation in cardiac biventricular geometries with outflow tracts, *International Journal for Numerical Methods in Biomedical Engineering* 35 (2019) e3185.
- [87] P. C. Franzone, L. F. Pavarino, S. Scacchi, *Mathematical Cardiac Electrophysiology*, volume 13, Springer, 2014.
- [88] K. H. ten Tusscher, A. V. Panfilov, Alternans and spiral breakup in a human ventricular tissue model, *American Journal of Physiology. Heart and Circulatory Physiology* 291 (2006) 1088–1100.
- [89] M. Courtemanche, R. J. Ramirez, S. Nattel, Ionic mechanisms underlying human atrial action potential properties: insights from a mathematical model, *American Journal of Physiology-Heart and Circulatory Physiology* 275 (1998) H301–H321.
- [90] A. Lee, U. Nguyen, O. Razeghi, J. Gould, B. Sidhu, B. Sieniewicz, J. Behar, M. Mafi-Rad, G. Plank, F. Prinzen, et al., A rule-based method for predicting the electrical activation of the heart with cardiac resynchronization therapy from non-invasive clinical data, *Medical Image Analysis* 57 (2019) 197–213.
- [91] F. Mazhar, F. Regazzoni, C. Bartolucci, C. Corsi, L. Dede', A. Quarteroni, S. Severi, Electro-Mechanical Coupling in Human Atrial Cardiomyocytes: Model Development and Analysis of Inotropic Interventions, in: *2021 Computing in Cardiology (CinC)*, volume 2021-Septe, IEEE, 2021, pp. 1–4. doi:10.23919/CinC53138.2021.9662766.
- [92] F. Regazzoni, L. Dedè, A. Quarteroni, Machine learning of multiscale active force generation models for the efficient simulation of cardiac electromechanics, *Computer Methods in Applied Mechanics and Engineering* 370 (2020) 113268.
- [93] R. Ogden, *Non-linear elastic deformations*, Dover Publications, 1997.
- [94] D. Guan, J. Yao, X. Luo, H. Gao, Effect of myofibre architecture on ventricular pump function by using a neonatal porcine heart model: from DT-MRI to rule-based methods, *Royal Society Open Science* 7 (2020) 191655.
- [95] T. P. Usyk, I. J. LeGrice, A. D. McCulloch, Computational model of three-dimensional cardiac electromechanics, *Computing and Visualization in Science* 4 (2002) 249–257.
- [96] M. Salvador, F. Regazzoni, S. Pagani, L. Dede', N. Trayanova, A. Quarteroni, The role of mechano-electric feedbacks and hemodynamic coupling in scar-related ventricular tachycardia, *Computers in Biology and Medicine* 142 (2022) 105203.
- [97] F. Regazzoni, L. Dedè, A. Quarteroni, Active force generation in cardiac muscle cells: mathematical modeling and numerical simulation of the actin-myosin interaction, *Vietnam Journal of Mathematics* 49 (2021) 87–118.
- [98] H. Jasak, Z. Tukovic, Automatic mesh motion for the unstructured finite volume method, *Transactions of FAMENA* 30 (2006) 1–20.
- [99] C. De Boor, *A practical Guide to Splines*, volume 27, springer-verlag New York, 1978.
- [100] J. Janela, A. Moura, A. Sequeira, Absorbing boundary conditions for a 3D non-Newtonian fluid–structure interaction model for blood flow in arteries, *International Journal of Engineering Science* 48 (2010) 1332–1349.

- [101] A. Quarteroni, T. Lassila, S. Rossi, R. Ruiz-Baier, Integrated heart—coupling multiscale and multiphysics models for the simulation of the cardiac function, *Computer Methods in Applied Mechanics and Engineering* 314 (2017) 345–407.
- [102] A. Quarteroni, *Numerical models for differential problems*, volume 16, Springer, 2018.
- [103] F. Regazzoni, A. Quarteroni, An oscillation-free fully partitioned scheme for the numerical modeling of cardiac active mechanics, *Computer Methods in Applied Mechanics and Engineering* 373 (2021) 113506.
- [104] F. Regazzoni, Stabilization of staggered time discretization schemes for 0D-3D fluid-structure interaction problems, *MOX report 17* (2022).
- [105] G. Rodriguez, *Smoothing and non-parametric regression*, Princeton University (2001).
- [106] D. Forti, L. Dedè, Semi-implicit BDF time discretization of the Navier–Stokes equations with VMS-LES modeling in a high performance computing framework, *Computers & Fluids* 117 (2015) 168–182.
- [107] Y. Bazilevs, V. Calo, J. Cottrell, T. Hughes, A. Reali, G. Scovazzi, Variational multiscale residual-based turbulence modeling for large eddy simulation of incompressible flows, *Computer Methods in Applied Mechanics and Engineering* 197 (2007) 173–201.
- [108] C. Bertoglio, A. Caiazzo, A tangential regularization method for backflow stabilization in hemodynamics, *Journal of Computational Physics* 261 (2014) 162–171.
- [109] S. Deparis, G. Grandperrin, A. Quarteroni, Parallel preconditioners for the unsteady Navier–Stokes equations and applications to hemodynamics simulations, *Computers & Fluids* 92 (2014) 253–273.
- [110] Z. M. G. Inc., *Zygote solid 3D heart generation ii developement report*. tech. rep. (2014).
- [111] L. Antiga, M. Piccinelli, L. Botti, B. Ene-Iordache, A. Remuzzi, D. A. Steinman, An image-based modeling framework for patient-specific computational hemodynamics, *Medical & Biological Engineering & Computing* 46 (2008) 1097–1112.
- [112] M. Fedele, A. M. Quarteroni, Polygonal surface processing and mesh generation tools for numerical simulations of the complete cardiac function, *International Journal for Numerical Methods in Biomedical Engineering* 37 (2021) e3435.
- [113] P. C. Africa, lifex: a flexible, high performance library for the numerical solution of complex finite element problems, *SoftwareX* 20 (2022) 101252.
- [114] P. C. Africa, R. Piersanti, M. Fedele, L. Dede’, A. Quarteroni, lifex-fiber: an open tool for myofibers generation in cardiac computational models, *BMC bioinformatics* 24 (2023) 143.
- [115] P. C. Africa, I. Fumagalli, M. Bucelli, A. Zingaro, M. Fedele, A. Quarteroni, et al., lifex-cfd: An open-source computational fluid dynamics solver for cardiovascular applications, *Computer Physics Communications* 296 (2024) 109039.
- [116] P. C. Africa, R. Piersanti, F. Regazzoni, M. Bucelli, M. Salvador, M. Fedele, S. Pagani, L. Dede’, A. Quarteroni, lifex-ep: a robust and efficient software for cardiac electrophysiology simulations, *BMC bioinformatics* 24 (2023) 389.
- [117] D. Arndt, W. Bangerth, B. Blais, M. Fehling, R. Gassmüller, T. Heister, L. Heltai, U. Köcher, M. Kronbichler, M. Maier, P. Munch, J.-P. Pelteret, S. Proell, K. Simon, B. Turcksin, D. Wells, J. Zhang, The deal.ii library, version 9.3, *J. Numer. Math.* 29 (2021).
- [118] D. Arndt, W. Bangerth, D. Davydov, T. Heister, L. Heltai, M. Kronbichler, M. Maier, J. Pelteret, B. Turcksin, D. Wells, The deal.II finite element library: design, features, and insights, *Computers & Mathematics with Applications* (2020).
- [119] Pulmonary acceleration time to estimate pulmonary pressure, visited: October 2022. URL: <https://www.dealii.org/>.
- [120] M. H. Crawford, C. A. Roldan, Quantitative assessment of valve thickness in normal subjects by trans-esophageal echocardiography, *The American Journal of Cardiology* 87 (2001) 1419–1423.

- [121] T. Gerach, S. Schuler, J. Fröhlich, L. Lindner, E. Kovacheva, R. Moss, E. M. Wülfers, G. Seemann, C. Wieners, A. Loewe, Electro-mechanical whole-heart digital twins: a fully coupled multi-physics approach, *Mathematics* 9 (2021) 1247.
- [122] L. Feng, H. Gao, X. Luo, Whole-heart modelling with valves in a fluid–structure interaction framework, *Computer Methods in Applied Mechanics and Engineering* 420 (2024) 116724.
- [123] P. van Ooij, M. Markl, J. D. Collins, J. C. Carr, C. Rigsby, R. O. Bonow, S. C. Malaisrie, P. M. McCarthy, P. W. Fedak, A. J. Barker, Aortic valve stenosis alters expression of regional aortic wall shear stress: New insights from a 4-dimensional flow magnetic resonance imaging study of 571 subjects, *Journal of the American Heart Association* 6 (2017) e005959.
- [124] W. Kriz, M. Elger, *Renal anatomy*, *Comprehensive clinical nephrology*. 3rd ed. Philadelphia (2010) 1–11.
- [125] A. M. Maceira, S. K. Prasad, M. Khan, D. J. Pennell, Normalized left ventricular systolic and diastolic function by steady state free precession cardiovascular magnetic resonance, *Journal of Cardiovascular Magnetic Resonance* 8 (2006) 417–426.
- [126] L. E. Hudsmith, S. E. Petersen, J. M. Francis, M. D. Robson, S. Neubauer, Normal human left and right ventricular and left atrial dimensions using steady state free precession magnetic resonance imaging, *Journal of Cardiovascular Magnetic Resonance* 7 (2005) 775–782.
- [127] A. M. Maceira, S. K. Prasad, M. Khan, D. J. Pennell, Reference right ventricular systolic and diastolic function normalized to age, gender and body surface area from steady-state free precession cardiovascular magnetic resonance, *European Heart Journal* 27 (2006) 2879–2888.
- [128] S. Clay, K. Alfakih, A. Radjenovic, T. Jones, J. P. Ridgway, Normal range of human left ventricular volumes and mass using steady state free precession mri in the radial long axis orientation, *Magnetic Resonance Materials in Physics, Biology and Medicine* 19 (2006) 41–45.
- [129] B. E. U. Burkhardt, C. J. Kellenberger, F. D. Franzoso, J. Geiger, A. Oxenius, E. R. Valsangiacomo Buechel, Right and left ventricular strain patterns after the atrial switch operation for d-transposition of the great arteries—a magnetic resonance feature tracking study, *Frontiers in Cardiovascular Medicine* 6 (2019) 39.
- [130] K. Hammermeister, R. Brooks, J. Warbasse, The rate of change of left ventricular volume in man: I. validation and peak systolic ejection rate in health and disease, *Circulation* 49 (1974) 729–738.
- [131] T. Sugimoto, R. Dulgheru, A. Bernard, F. Ilardi, L. Contu, K. Addetia, L. Caballero, N. Akhaladze, G. D. Athanassopoulos, D. Barone, et al., Echocardiographic reference ranges for normal left ventricular 2d strain: results from the eacvi norre study, *European Heart Journal-Cardiovascular Imaging* 18 (2017) 833–840.
- [132] A. Bishop, P. White, P. Oldershaw, R. Chaturvedi, C. Brookes, A. Redington, Clinical application of the conductance catheter technique in the adult human right ventricle, *International journal of cardiology* 58 (1997) 211–221.
- [133] L. Thomas, E. Foster, N. B. Schiller, Peak mitral inflow velocity predicts mitral regurgitation severity, *Journal of the American College of Cardiology* 31 (1998) 174–179.
- [134] G. Di Labbio, L. Kadem, Jet collisions and vortex reversal in the human left ventricle, *Journal of Biomechanics* 78 (2018) 155–160.
- [135] P. J. Kilner, G.-Z. Yang, A. J. Wilkes, R. H. Mohiaddin, D. N. Firmin, M. H. Yacoub, Asymmetric redirection of flow through the heart, *Nature* 404 (2000) 759–761.
- [136] F. C. Bueno, I. Rodríguez-Bailón, R. López-Salguero, J. J. Gómez-Doblas, J. M. García-Pinilla, E. de Teresa Galván, Effect of exercise on systolic left ventricular outflow velocity in healthy adults, *Revista Española de Cardiología (English Edition)* 59 (2006) 180–182.
- [137] J.-O. Choi, M.-S. Shin, M.-J. Kim, H. O. Jung, J. R. Park, I. S. Sohn, H. Kim, S.-M. Park, N. J. Yoo, J. H. Choi, et al., Normal echocardiographic measurements in a korean population study: part ii. doppler and tissue doppler imaging, *Journal of Cardiovascular Ultrasound* 24 (2016) 144–152.

- [138] Pulmonary acceleration time to estimate pulmonary pressure, visited: October 2022. URL: <https://123sonography.com/ebook/pulmonary-acceleration-time-to-estimate-pulmonary-pressure>.
- [139] Normal pressures in the heart and great vessels, Accessed: October 2022. URL: <https://www.msmanuals.com/professional/multimedia/table/normal-blood-pressure-in-the-heart-and-great-vessels>.
- [140] L. Littmann, J. D. Symanski, Hemodynamic implications of left bundle branch block, *Journal of Electrocardiology* 33 (2000) 115–121.
- [141] J. Eriksson, J. Zajac, U. Alehagen, A. F. Bolger, T. Ebbers, C.-J. Carlhäll, Left ventricular hemodynamic forces as a marker of mechanical dyssynchrony in heart failure patients with left bundle branch block, *Scientific Reports* 7 (2017) 1–9.
- [142] M. Alessandrini, M. De Craene, O. Bernard, S. Giffard-Roisin, P. Allain, I. Waechter-Stehle, J. Weese, E. Saloux, H. Delingette, M. Sermesant, et al., A pipeline for the generation of realistic 3d synthetic echocardiographic sequences: Methodology and open-access database, *IEEE transactions on Medical Imaging* 34 (2015) 1436–1451.
- [143] J. C. DILLON, S. CHANG, H. FEIGENBAUM, Echocardiographic manifestations of left bundle branch block, *Circulation* 49 (1974) 876–880.
- [144] O. Gjesdal, E. W. Remme, A. Opdahl, H. Skulstad, K. Russell, E. Kongsgaard, T. Edvardsen, O. A. Smiseth, Mechanisms of abnormal systolic motion of the interventricular septum during left bundle-branch block, *Circulation: Cardiovascular Imaging* 4 (2011) 264–273.
- [145] M. Strocchi, S. Longobardi, C. M. Augustin, M. A. Gsell, A. Petras, C. A. Rinaldi, E. J. Vigmond, G. Plank, C. J. Oates, R. D. Wilkinson, et al., Cell to whole organ global sensitivity analysis on a four-chamber heart electromechanics model using gaussian processes emulators, *PLOS Computational Biology* 19 (2023) e1011257.
- [146] F. Regazzoni, M. Salvador, L. Dedè, A. Quarteroni, A machine learning method for real-time numerical simulations of cardiac electromechanics, *Computer methods in applied mechanics and engineering* 393 (2022) 114825.
- [147] S. Longobardi, A. Lewalle, S. Coveney, I. Sjaastad, E. K. Espe, W. E. Louch, C. J. Musante, A. Sher, S. A. Niederer, Predicting left ventricular contractile function via gaussian process emulation in aortic-banded rats, *Philosophical Transactions of the Royal Society A* 378 (2020) 20190334.
- [148] M. Salvador, M. Strocchi, F. Regazzoni, L. Dede, S. Niederer, A. Quarteroni, Real-time whole-heart electromechanical simulations using latent neural ordinary differential equations, *arXiv preprint arXiv:2306.05321* (2023).
- [149] The American Society of Mechanical Engineers, Assessing Credibility of Computational Modeling through Verification and Validation: Application to Medical Devices VV 40 - 2018, Technical Report, 2018.
- [150] U.S. Department of Health and Human Services, Food and Drug Administration, Center for Devices and Radiological Health, Assessing the Credibility of Computational Modeling and Simulation in Medical Device Submissions, Technical Report, 2023.
- [151] S. A. Niederer, E. Kerfoot, A. P. Benson, M. O. Bernabeu, O. Bernus, C. Bradley, E. M. Cherry, R. Clayton, F. H. Fenton, A. Garny, et al., Verification of cardiac tissue electrophysiology simulators using an n-version benchmark, *Philosophical Transactions of the Royal Society A: Mathematical, Physical and Engineering Sciences* 369 (2011) 4331–4351.
- [152] M. Hirschvogel, M. Bassilious, L. Jagschies, S. M. Wildhirt, M. W. Gee, A monolithic 3d-0d coupled closed-loop model of the heart and the vascular system: Experiment-based parameter estimation for patient-specific cardiac mechanics, *International Journal for Numerical Methods in Biomedical Engineering* 33 (2017) e2842.